A robust approach to time-to-depth conversion and interval velocity estimation from time migration in the presence of lateral velocity variations[a]

[a]Published in Geophysical Prospecting, 63, no. 2, 315-337, (2015)

Siwei Li and Sergey Fomel

ABSTRACT

The problem of conversion from time-migration velocity to an interval velocity in depth in the presence of lateral velocity variations can be reduced to solving a system of partial differential equations. In this paper, we formulate the problem as a nonlinear least-squares optimization for seismic interval velocity and seek its solution iteratively. The input for inversion is the Dix velocity which also serves as an initial guess. The inversion gradually updates the interval velocity in order to account for lateral velocity variations that are neglected in the Dix inversion. The algorithm has a moderate cost thanks to regularization that speeds up convergence while ensuring a smooth output. The proposed method should be numerically robust compared to the previous approaches, which amount to extrapolation in depth monotonically. For a successful time-to-depth conversion, image-ray caustics should be either nonexistent or excluded from the computational domain. The resulting velocity can be used in subsequent depth-imaging model building. Both synthetic and field data examples demonstrate the applicability of the proposed approach.

INTRODUCTION

Time-domain seismic processing has been a popular and effective tool in areas with mild lateral velocity variations (Yilmaz, 2001; Robein, 2003; Bartel et al., 2006). Time migration produces images in the time coordinate as opposed to the usual depth coordinate. The time coordinate, along with time-migration velocities, is determined during time migration by optimizing image qualities. However, it is highly sensitive to lateral velocity changes (Black and Brzostowski, 1994; Bevc et al., 1995). Therefore, the time-migrated image is usually distorted (Hubral, 1977; Cameron et al., 2007, 2008, 2009; Iversen and Tygel, 2008). For this reason, in many cases time migrations are inadequate for accurate geological interpretation of subsurface structures. On the other hand, time-migration velocities can be conveniently and efficiently estimated either by repeated migrations (Yilmaz et al., 2001) or by velocity continuation (Fomel,

2003). Depth migration can handle general media and output images in regular Cartesian depth coordinates. But it requires an accurate interval velocity model construction, which is in practice both challenging and time-consuming. An iterative process of tomographic updates is often employed (Bishop et al., 1985; Stork and Clayton, 1992), where a good initial interval velocity model is crucial for achieving the global minimum. It is thus of great interest to convert the time-migration velocity to the depth domain in order to unravel inherent distortions in time-domain images and to provide a reasonable starting model for building depth-imaging velocities.

The relationship between time and depth coordinates was first explained by Hubral (1977) through the concept of *image rays*. An interval velocity model can be converted to one in the time domain by tracing image rays that dive into earth with slowness vector normal to the surface. The time coordinates are then defined by the traveltime along image rays and its surface location (Larner et al., 1981; Robein, 2003). However this process is not trivially revertible and it does not reveal directly the connection between time-migration velocity and interval velocity. According to Dix (1955), in a layered medium where $v = v(z)$, the image rays run straightly downward and the time-migration velocities are the root-mean-square (RMS) velocities appearing in a truncated Taylor approximation for traveltimes. The Dix inversion formula is exact in a $v(z)$ medium, where the conversion between time- and depth-domain attributes is theoretically straightforward.

Even a mild lateral velocity variation can cause image rays to bend and invalidate Dix inversion. Cameron et al. (2007, 2008) studied and established theoretical relations between the time-migration velocity and the seismic velocity in depth for general media using the paraxial ray-tracing theory. They showed that the conventional Dix velocity is equal to the ratio of the interval velocity and the geometrical spreading of image rays. This is consistent with Dix formula because when $v = v(z)$ the geometrical spreading equals to one everywhere. In order to carry out the time-to-depth conversion in the presence of lateral velocity variations, one can solve a nonlinear partial differential equation (PDE) of elliptic type with boundary conditions on the surface (Cameron et al., 2009). The problem is mathematically ill-posed. Cameron et al. (2009) adopt a two-step numerical procedure for the time-to-depth conversion. The first step is a Lax-Friedrichs-like finite-difference method or a spectral Chebyshev method to solve for geometrical spreading in the time coordinate. The next step is a Dijkstra-like solver motivated by the fast marching method (Sethian, 1999) for velocity conversion and coordinate mapping. In this approach, it is crucial to yield the development of low harmonics and damp the high harmonics during the first stage. Iversen and Tygel (2008) discussed an extension of the time-to-depth conversion problem along 2-D profiles in 3-D. An essential part of the algorithm is the time-stepping (integration) along image-rays. The robustness of these methods may not be satisfactory in practice because of stability issues that arise from the ill-posed nature of the problem.

In this paper, we start with the theoretical relations derived by Cameron et al. (2007, 2008) but cast the original problem in a nonlinear iterative optimization frame-

work. This idea is motivated by the observation that, for arbitrary depth velocity model, two of the PDEs can be always satisfied, while the remaining one associated with image-ray geometrical spreading can be rewritten in the form of a cost functional that indicates errors in interval velocity. A key benefit in our formulation is that each iteration will give a global update of the whole velocity model. In contrast, the previous approaches only consider information locally at each time step. Another advantage is that we are able to include regularization in the optimization framework in order to deal with the ill-posedness issue.

The paper is organized as follows. We first show theoretical derivations of all necessary components involved in the proposed approach. Next, we develop a numerical implementation for 2-D time-to-depth conversion. Finally, we test the algorithm on synthetic and field data examples. We conclude the paper by giving some discussions on the proposed method.

THEORY

For completeness, we will first review some basic concepts related to time-to-depth conversion. Then we show the theoretical derivation for an optimization formulation of the problem and a corresponding inversion procedure. For simplicity, we restrict our analysis below to the 2-D case.

Connection between time- and depth-domain attributes

In Figure 1, we illustrate image rays in 2-D and a *forward* mapping from depth coordinate (z, x) to time coordinate (t_0, x_0) (Hubral, 1977). Throughout this paper t_0 stands for one-way time, while time migration usually produces images in two-way time (Yilmaz, 2001), i.e. $(2t_0, x_0)$. Under the assumption of no caustics, for each subsurface location (z, x) we consider the image ray from (z, x) to the surface, where it emerges at point $(0, x_0)$, with slowness vector normal to the surface. Here x_0 is the location of the image ray at the earth surface and is a scalar. t_0 is the traveltime along this image ray between (z, x) and $(0, x_0)$. The forward mapping $t_0(z, x)$ and $x_0(z, x)$ can be done with a knowledge of interval velocity $v(z, x)$. A unique *inverse* mapping $z(t_0, x_0)$ and $x(t_0, x_0)$ also exists that enables us to directly map the time-migrated image to depth.

The counterpart for $v(z, x)$ in the time-domain is the time-migration velocity $v_m(t_0, x_0)$, which is commonly estimated in prestack Kirchhoff time migration (Yilmaz, 2001; Fomel, 2003). In a $v(z)$ medium, v_m corresponds to the root-mean-square (RMS) velocity:

$$v_m(t_0) = \sqrt{\frac{1}{t_0}\int_0^{t_0} v^2(z(t))\,dt}\;. \tag{1}$$

A time-to-depth velocity conversion can be done by first applying the Dix inversion

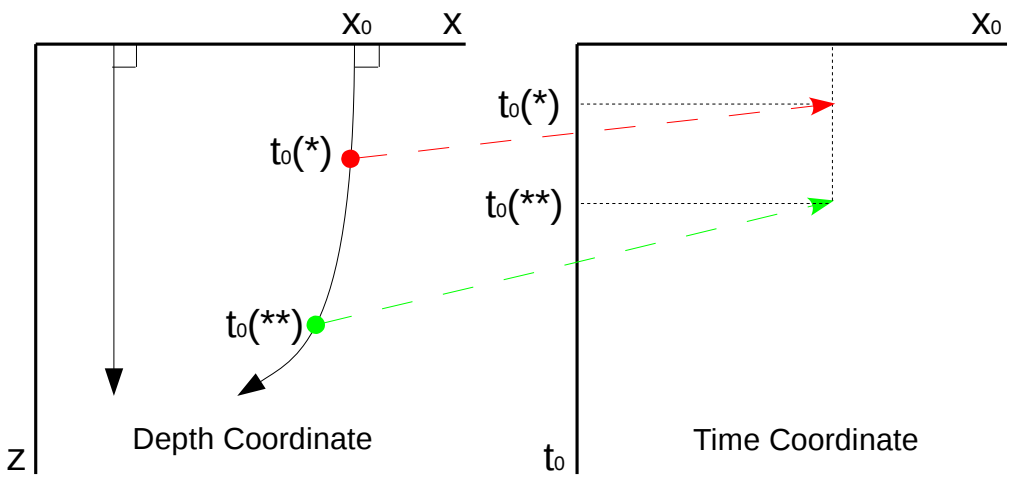

Figure 1: Image ray in (left) the depth-domain can be traced with a source at location x_0 with slowness vector normal to the earth surface. Each depth coordinate (z, x) along this image ray is then mapped into (right) the time coordinate (t_0, x_0) by using its corresponding traveltime t_0 and source location x_0.

formula (Dix, 1955), which is theoretically exact in this case:

$$v_d(t) = \sqrt{\frac{d}{dt_0}(t_0 v_m^2(t_0))}\ , \tag{2}$$

followed by performing a simple conversion from $v_d(t)$ to $v(z)$ according to $z = \frac{1}{2}\int_0^t v_d(t)dt$.

In equations 1 and 2, there is no dependency on x_0 or x, because image rays are all vertical. For an arbitrary medium, image rays will bend as they travel through the medium (Larner et al., 1981). Therefore, in general, v_m is a function of both t_0 and x_0 and no longer satisfies the simple expression 1, which limits the applicability of the Dix formula. Cameron et al. (2007) proved that the seismic velocity and the Dix velocity in this case are connected through geometrical spreading Q of image rays:

$$v_d(t_0, x_0) \equiv \sqrt{\frac{\partial}{\partial t_0}(t_0 v_m^2(t_0, x_0))} = \frac{v(z(t_0, x_0), x(t_0, x_0))}{Q(t_0, x_0)}\ . \tag{3}$$

In equation 3, the generalized Dix velocity is defined by Cameron et al. (2007) in a way similar to equation 2 with a change from d/dt_0 to a partial differentiation with respect to t_0. The quantity Q is related to $x_0(z, x)$ using its definition (Popov, 2002; Cameron et al., 2007), as follows:

$$|\nabla x_0|^2 = \frac{1}{Q^2}\ . \tag{4}$$

Combining equations 3 and 4 results in

$$|\nabla x_0(z,x)|^2 = \frac{v_d^2(t_0(z,x),x_0(z,x))}{v^2(z,x)} \; . \tag{5}$$

The traveltimes along image rays obey the eikonal equation (Hubral, 1977; Chapman, 2004), thus

$$|\nabla t_0(z,x)|^2 = \frac{1}{v^2(z,x)} \; . \tag{6}$$

Finally, since x_0 remains constant along each image ray, there is an orthogonality condition between gradients of t_0 and x_0 (Cameron et al., 2007):

$$\nabla t_0(z,x) \cdot \nabla x_0(z,x) = 0 \; . \tag{7}$$

Equations 5, 6 and 7 form a system of nonlinear PDEs for $t_0(z,x)$ and $x_0(z,x)$. The input is $v_d(t_0,x_0)$, estimated from $v_m(t_0,x_0)$ by equation 3. Solving a boundary-value problem for the PDEs should provide $v(z,x)$, as well as $t_0(z,x)$ and $x_0(z,x)$. Because seismic acquisitions are limited to the earth surface, we can only use boundary conditions at the surface. For a rectangular Cartesian domain with $z=0$ being the surface, the boundary conditions are

$$\left\{ \begin{array}{rcl} t_0(0,x) & = & 0 \; , \\ x_0(0,x) & = & x \; . \end{array} \right. \tag{8}$$

In Appendix A, we show that the time-to-depth conversion is an ill-posed problem because it requires solving a Cauchy-type problem for an elliptic PDE. The missing boundary conditions on sides of the computational domain other than those in equation 8 can induce numerical instability when extrapolating in t_0 (or, equivalently, z). Instead, we consider an alternative formulation of the problem in the following section.

The optimization formulation

Given boundary conditions 8, equation 6 describes the traveltime t_0 of a velocity model with a plane-wave source at the surface. For a given t_0, equation 7 is a first-order linear PDE on x_0 and thus computation of x_0 is straightforward. Our idea is inspired by a natural logic: if the resulting x_0 does not satisfy equation 5, we need to modify v in a way such that the misfit decreases, and repeat the process until convergence.

Mathematically, we define a cost function $f(z,x)$ based on equation 5:

$$f(z,x) = \nabla x_0 \cdot \nabla x_0 - v_d^2 \, w \; , \tag{9}$$

where for convenience we use slowness-squared $w(z,x) = v^{-2}(z,x)$ instead of v. Note that f is dimensionless. The discretized form of equation 9 reads

$$\mathbf{f} = (\nabla \mathbf{x_0} \cdot \nabla)\, \mathbf{x_0} - \mathrm{diag}(\mathbf{v_d} \star \mathbf{v_d})\, \mathbf{w} \equiv \mathbf{L}_{x_0}\, \mathbf{x_0} - \mathrm{diag}(\mathbf{v_d} \star \mathbf{v_d})\, \mathbf{w} \ . \tag{10}$$

In equation 10, $\mathbf{f}, \mathbf{x_0}, \mathbf{v_d}$ and $\mathbf{w}$ are all column vectors after discretizing the computational domain (z,x). For example, $\mathbf{x_0}$ is the discretized column vector of $x_0(z,x)$. The vector $\mathbf{v_d}$ may require interpolation because it is in (t_0, x_0) while the discretization is in (z,x). The interpolation can be done after forward mapping from (z,x) to (t_0,x_0) at current velocity model. We denote an operator which is a matrix $\mathbf{L}_{x_0} = \nabla \mathbf{x_0} \cdot \nabla$. The other operator diag() expands a vector into a diagonal matrix. Finally, the symbol $\star$ stands for an element-wise vector-vector multiplication.

As is common in many optimization problems, we seek to minimize the least-squares norm of $\mathbf{f}$:

$$E[\mathbf{w}] = \frac{1}{2}\|\mathbf{f}\|^2 = \frac{1}{2}\mathbf{f}^T\mathbf{f} \ , \tag{11}$$

where the superscript T stands for transpose. The Gauss-Newton method in optimization requires linearizing the cost function in equation 10:

$$\frac{\partial f}{\partial w} = 2\,(\nabla x_0 \cdot \nabla)\,\frac{\partial x_0}{\partial w} - 2\,v_d\,w\,\frac{\partial v_d}{\partial w} - v_d^2 \ . \tag{12}$$

The Fréchet derivative matrix $\mathbf{J}$ required by inversion is the discretized form of equation 12, i.e., $\mathbf{J} = \partial \mathbf{f}/\partial \mathbf{w}$. In Appendix B we find that $\mathbf{J}$ is a cascade and summation of several parts. An update $\delta\mathbf{w}$ at current $\mathbf{w}$ is found by solving the following normal equation arising from the Gauss-Newton approach (Björck, 1996):

$$\delta\mathbf{w} = \left[\mathbf{J}^T\mathbf{J}\right]^{-1}\mathbf{J}^T(-\mathbf{f}) \ . \tag{13}$$

Equations 11 and 13 together suggest a nonlinear inversion procedure for solving the original system of PDEs 5, 6 and 7. The inversion is analogous to traveltime tomography but with more complexity. The cost 9 can be interpreted as difference between modeled and observed geometrical spreadings. However, both of them depend on the model v, while in traveltime tomography the observed arrival times are independent of v. The forward modeling in our case involves two steps, which construct a curvilinear coordinate system that is sensitive to lateral velocity variations. On the other hand, the forward modeling in traveltime tomography consists of only one step. Last but not least, unlike traveltime tomography, we have observations everywhere in the computational domain, except for areas excluded due to instabilities of the numerical implementation, as we will discuss later.

Before introducing a numerical implementation, we would like to point out several important facts and assumptions that make a successful time-to-depth conversion possible by the proposed method:

- Caustics must be excluded from the computational domain. In regions where caustics develop, the gradient ∇x_0 goes to infinity and the cost function is not

well-defined. For all numerical examples in this paper, we do not encounter this issue. In the Discussion section, we provide a possible strategy to cope with this limitation.

- According to derivations in Appendix B, the calculation of $\delta\mathbf{w}$ depends on values of $\partial\mathbf{v_d}/\partial\mathbf{t_0}$ and $\partial\mathbf{v_d}/\partial\mathbf{x_0}$. Thus the input v_d should be differentiable. This requirement can be satisfied during v_m estimation by using regularization (Fomel, 2003).

- Similarly to all nonlinear inversions, the proposed method requires a prior model that is sufficiently close to desired model at the global minimum $E = 0$. Meanwhile, to guarantee stability and a smooth output, some form of regularization should be imposed during inversion (Engl et al., 1996; Zhdanov, 2002).

- Our formulation does not change the ill-posed nature of the original problem. One assumption is that condition 8 describes all *in-flow* domain boundaries of t_0 and x_0. In other words, the image rays are only allowed to be either parallel to or exiting (*out-flow*) all other boundaries of the computational domain except the surface.

For the prior model, we adopt the Dix-inverted model. In other words, we seek to refine the interval velocity given by equation 2 by taking the geometrical spreading of image rays into consideration according to equation 3.

NUMERICAL IMPLEMENTATION

Below we outline the steps involved in computing one linearization update:

1. Given current $v(z, x)$, solve equation 6 for $t_0(z, x)$ with $t_0(0, x) = 0$;
2. Given $t_0(z, x)$ and $x_0(0, x) = x$, solve equation 7 for $x_0(z, x)$;
3. Given $t_0(z, x)$ and $x_0(z, x)$, interpolate $v_d(z, x)$ from $v_d(t_0, x_0)$ and compute $f(z, x)$ based on equation 9;
4. Assemble linear operator B-5 and solve equation 13 for $\delta w(z, x)$.

First, we apply the fast-marching method (Sethian, 1999; Sethian and Popovici, 1999) to solve the eikonal equation 6 by initializing a plane-wave source at $z = 0$. Computation for x_0 can be incorporated into t_0 by adopting the upwind finite-differences of t_0 for equation 7. In Figure 2, consider a currently updated grid point C during forward modeling of t_0. If it has only one upwind neighbor A that is inside the wave-front, $t_0(C) > t_0(A)$, then the image ray must be aligned with grid segment AC and therefore $x_0(C) = x_0(A)$. We refer to this scenario as one-sided. If C has two upwind neighbors A and B, $t_0(C) > \max\{t_0(A), t_0(B)\}$, and they are both inside

the wave-front, then the image ray must intersect the simplex ABC from an angle. In this case, we compute $x_0(C)$ from

$$\frac{(t_0(C)-t_0(A))(x_0(C)-x_0(A))}{h_z^2}+\frac{(t_0(C)-t_0(B))(x_0(C)-x_0(B))}{h_x^2}=0\,. \qquad (14)$$

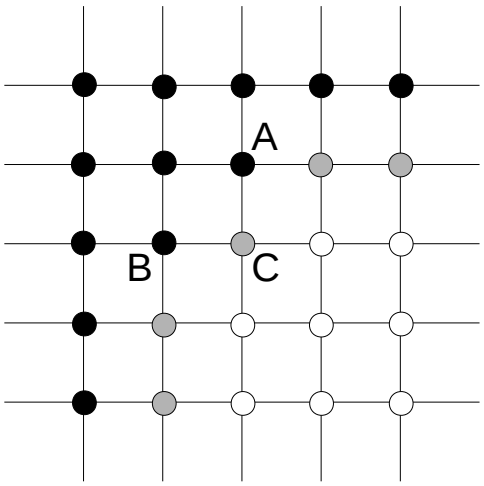

Figure 2: A modified fast-marching method for forward modeling. Black dots represent region that has been swept by the wave-front, gray dots are the expanding wave-front and grid points being updated, and white dots are region yet to be reached.

Because $\mathbf{x_0}$ at certain grid points is calculated by one-sided scenario, $\mathbf{L}_{x_0}$ there contains all zeros. Consequently, an evaluation of the cost $\mathbf{f}$ at these locations with $\mathbf{L}_{x_0}\,\mathbf{x_0}$ becomes inaccurate. We exclude these regions from $\mathbf{f}$ and expect inversion to fill them.

Next, we apply simple bilinear interpolation for $v_d(z,x)$ and estimate $\delta\mathbf{w}$ by solving equation 13 using shaping regularization (Fomel, 2007). We use a triangular smoother with adjustable size as the shaping operator. We find in numerical tests that shaping significantly improves convergence speed compared to that of the traditional Tikhonov regularization (Tikhonov, 1963) with gradient operators. We also observe that without regularization the model update can be undesirably oscillatory. We believe this phenomenon is related to the ill-posedness of the PDEs.

Finally, we reduce computational cost by adopting the method of conjugate gradients (Hestenes and Stiefel, 1952) and an efficient implementation of $\mathbf{J}$, as well as its adjoint, according to the equations derived in Appendix B. For this purpose, we choose the upwind finite-difference scheme (Franklin and Harris, 2001; Li et al., 2011)

based on $\mathbf{t_0}$ for both $\mathbf{L}_{t_0}$ and $\mathbf{L}_{x_0}$. As shown by Li et al. (2013), applying $\mathbf{J}$ and its transpose involves only sparse triangularized matrix-vector multiplications and is therefore inexpensive. For example, at each grid point $\mathbf{L}_{t_0}^{-1}$ relies on only its upwind neighbors. The computational complexity of $\mathbf{J}$ and $\mathbf{J}^T$ is $O(N)$, where N is the total number of grid points.

EXAMPLES

Constant velocity gradient model

In a medium with a constant velocity gradient

$$v(z,x) = v_0 + g_z z + g_x x \ , \tag{15}$$

image rays are segments of circles parallel to each other, and all attributes involved in time-to-depth conversion have analytical solutions. In Appendix C, we derive the following relationships:

$$x_0(z,x) = x + \frac{\sqrt{(v_0+g_x x)^2 + g_x^2 z^2} - (v_0 + g_x x)}{g_x} \ , \tag{16}$$

$$t_0(z,x) = \frac{1}{g}\text{arccosh}\left[\frac{g^2\left(\sqrt{(v_0+g_x x)^2 + g_x^2 z^2} + g_z z\right) - v g_z^2}{v g_x^2}\right] \ , \tag{17}$$

where $g = \sqrt{g_z^2 + g_x^2}$. The migration velocity v_m and Dix velocity v_d take the following expressions:

$$v_m(t_0,x_0) = \frac{(v_0 + g_x x_0)^2}{t_0\left(g\coth(g t_0) - g_z\right)} \ , \tag{18}$$

$$v_d(t_0,x_0) = \frac{(v_0 + g_x x_0) g}{g\cosh(g t_0) - g_z \sinh(g t_0)} \ . \tag{19}$$

It is easy to verify from equations 16 and 17 that $|\nabla x_0| = 1$, $|\nabla t_0| = 1/v$ and $\nabla x_0 \cdot \nabla t_0 = 0$. Because there is no geometrical spreading of image rays in this case, the Dix velocity will be equal to the interval velocity according to equation 3. However, a Dix-inverted model will still be distorted if $g_x \neq 0$ because of the lateral shift of image rays.

Figures 3 and 4 show a velocity model with $v(z,x) = 1.5 + 0.75z + 0.5x$ km/s and the corresponding analytical $v_d(t_0,x_0)$, $x_0(z,x)$ and $t_0(z,x)$. Clearly, the right domain boundary is of in-flow type that violates our assumption. To address this challenge, we include Dix velocity in regions beyond the original left and right boundaries during inversion, but mask out the cost in these regions. It means that the time-to-depth conversion is performed in a sub-domain of time-domain attributes, such that information on the in-flow boundary is available. Afterwards, we apply Dix inversion to

the expanded model and use the result as the prior model. We use the exact Dix velocity in equation 19 for evaluating the right-hand side of 5. Then, in total three linearization updates are carried out, which decreases E to relative 0.6%. The radiuses of triangular smoother in shaping are 8 m vertically and 30 m horizontally (8 m $\times$ 30 m). At last, we cut the computational domain back to its original size. Figures 5 and 6 compare the cost and model misfit before and after inversion.

We also synthesize data with Kirchhoff modeling (Haddon and Buchen, 1981) for several horizontal reflectors using the exact model, and examine the subsurface scattering-angle common-image-gathers from Kirchhoff prestack depth migration (Xu et al., 2001) as an evidence of interval velocity improvements. In Figure 7, the shallower events do not improve significantly because the image rays have not yet bent considerably. Deeper events become noticeably flatter after applying the proposed method.

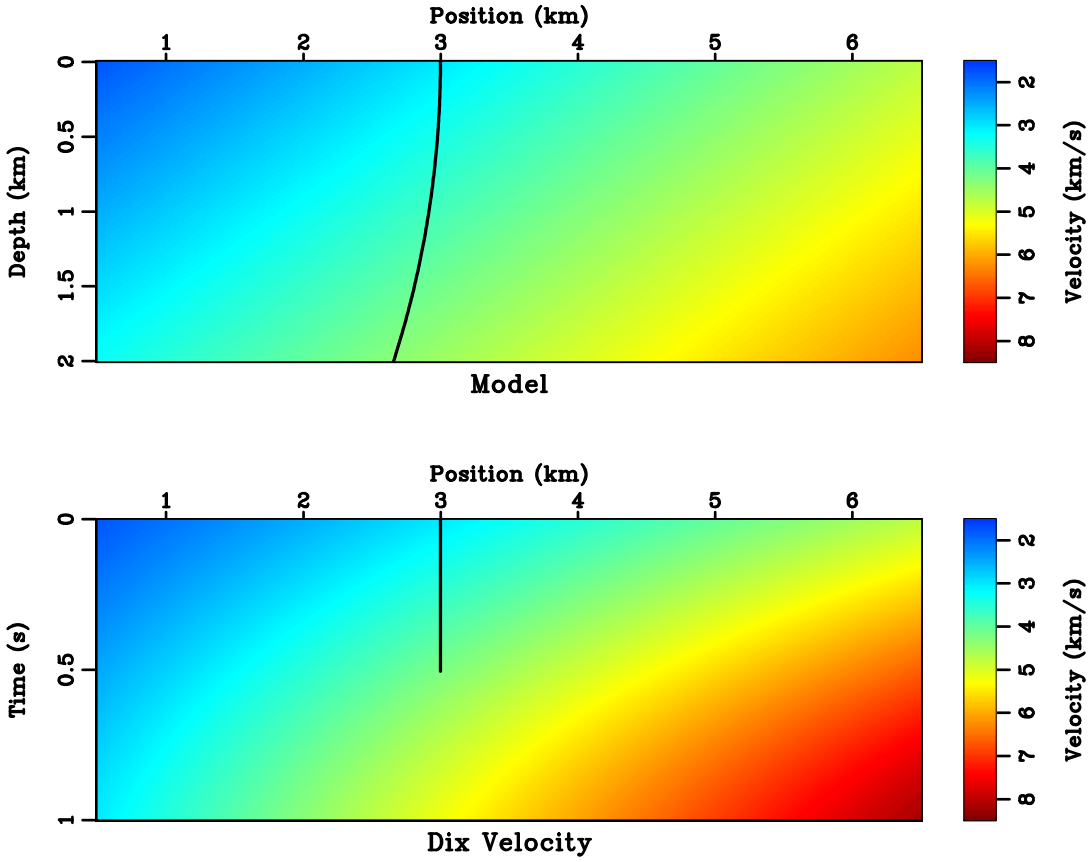

Figure 3: (Top) a constant velocity gradient model and (bottom) the analytical Dix velocity v_d. A curved image ray is mapped to the time domain as a straight line.

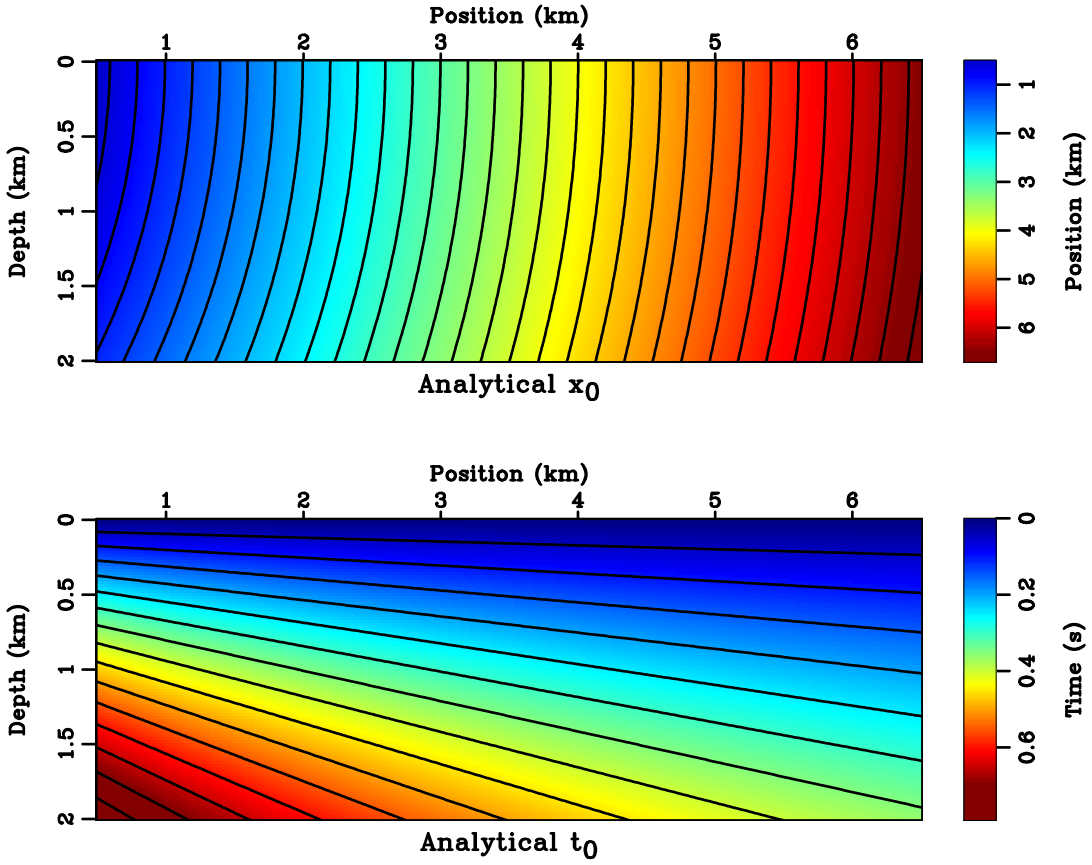

Figure 4: Analytical values of (top) t_0 and (bottom) x_0 of the model in Figure 3. Both figures are overlaid with contour lines that, according to equation 7, are perpendicular to each other. Each contour line of x_0 is an image ray, while the contours of t_0 illustrate the propagation of a plane-wave.

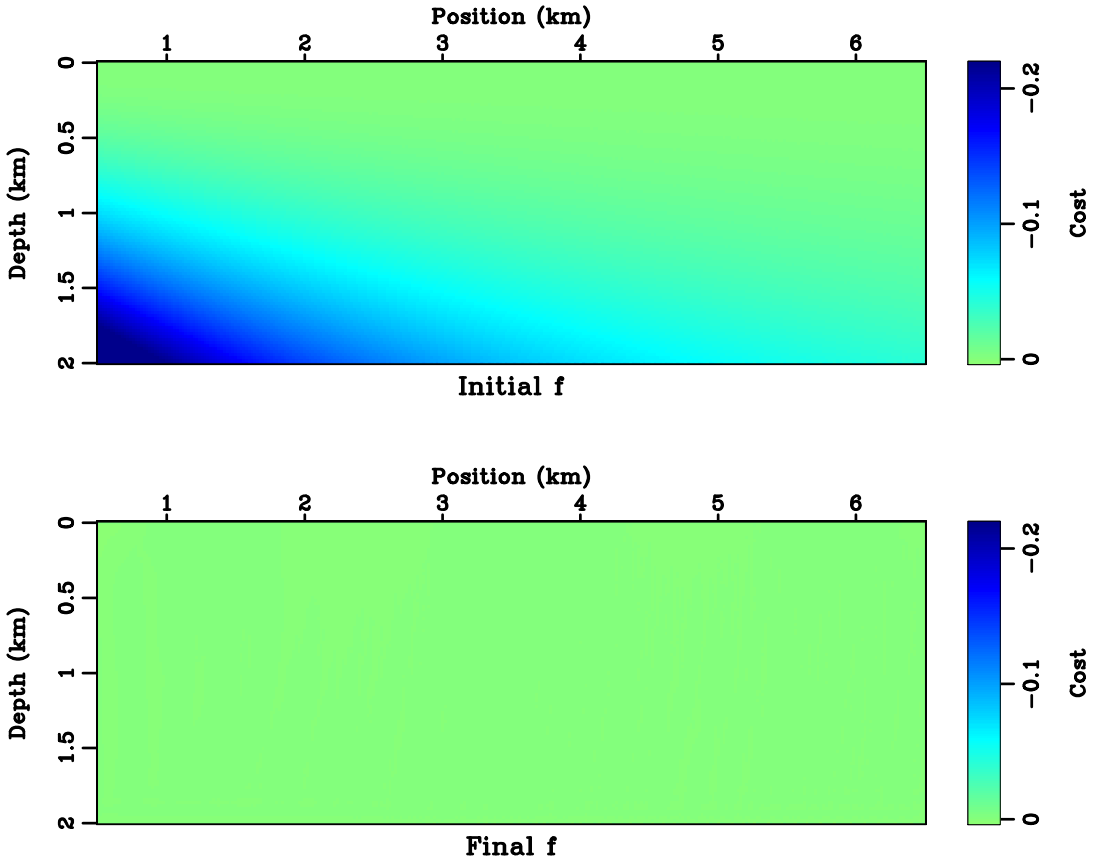

Figure 5: The cost defined by equation 9 (top) before and (bottom) after inversion. The least-squares norm of cost E is decreased from 9.855 to 0.057.

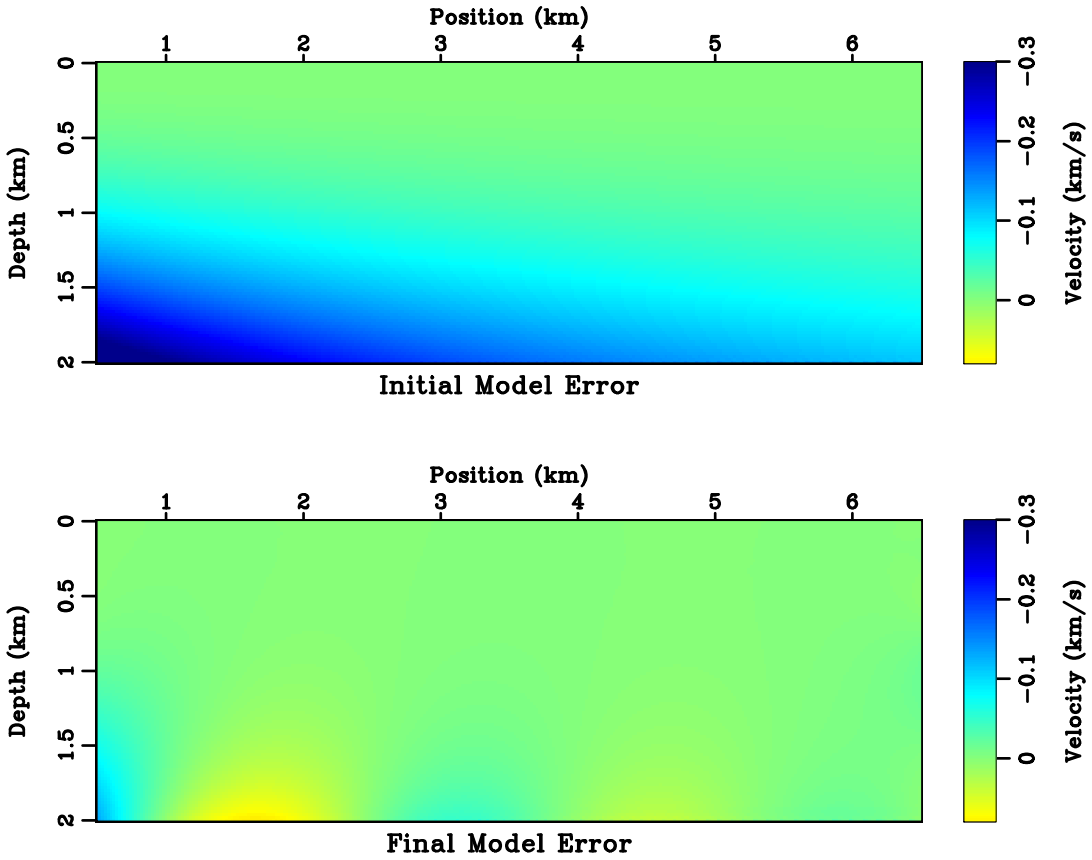

Figure 6: The difference between exact model and (top) initial model and (bottom) inverted model. The least-squares norm of model misfit is decreased from 15.6 km^2/s^2 to 2.7 km^2/s^2.

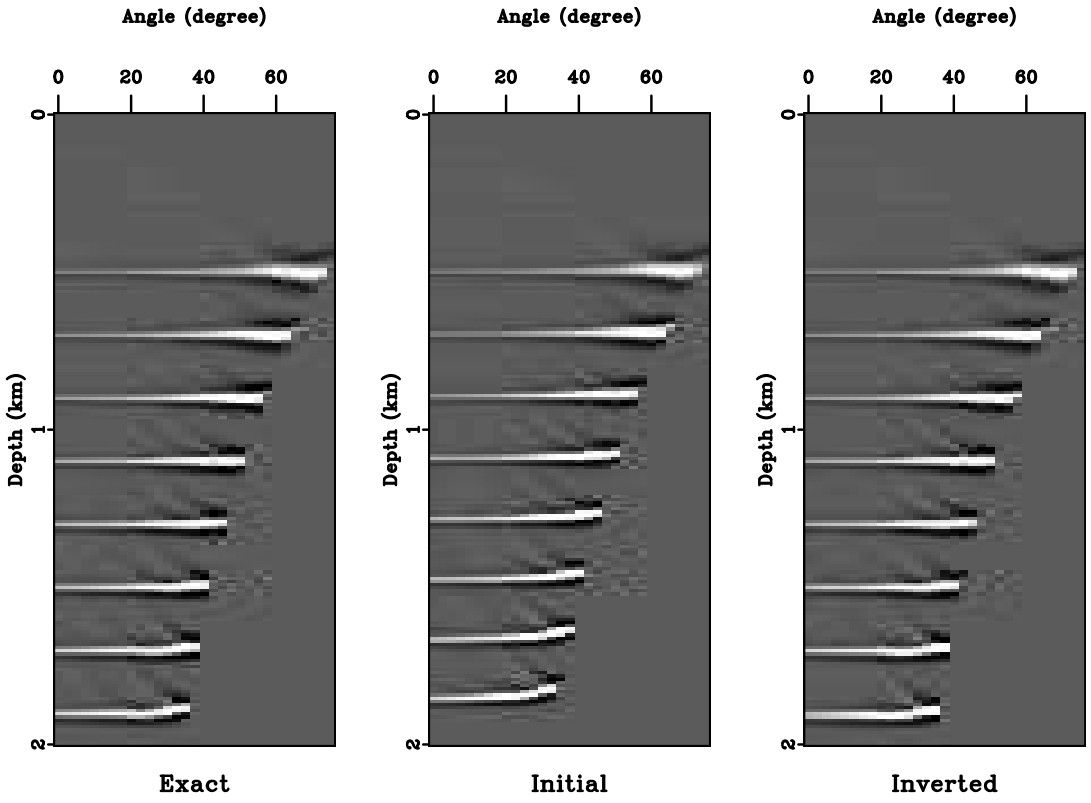

Figure 7: Comparison of the subsurface scattering-angle common-image-gathers at $x = 1.5$ km of (left) exact model, (middle) prior model and (right) inverted model.

Constant horizontal slowness-squared gradient model

Another medium that provides analytical time-to-depth conversion formulas is

$$w(z,x) = w_0 - 2q_x x \ , \tag{20}$$

i.e., the slowness-squared changes linearly in the horizontal direction. In Appendix D, we show that in this case the coordinate mapping follows

$$x_0(z,x) = \frac{2w_0 x + q_x z^2}{w_0 + 2q_x x + \sqrt{(w_0 - 2q_x x)^2 - 4q_x^2 z^2}} \ , \tag{21}$$

$$t_0(z,x) = \frac{\sqrt{2}z\left[2w_0 - 4q_x x + \sqrt{(w_0 - 2q_x x)^2 - 4q_x^2 z^2}\right]}{3\left[w_0 - 2q_x x + \sqrt{(w_0 - 2q_x x)^2 - 4q_x^2 z^2}\right]^{\frac{1}{2}}} \ . \tag{22}$$

The analytical expression for $v_d(t_0, x_0)$ is more complex and can be found in equations D-13 and D-14.

In Figure 8 we illustrate $x_0(z,x)$ and $t_0(z,x)$ in the model $w(z,x) = 1 - 0.052x$ $\mathrm{s}^2/\mathrm{km}^2$. To deal with the in-flow boundary issue, we apply the method described previously for the constant velocity gradient example. Unlike equation 16, equation 21 indicates varying geometrical spreadings in the domain. Figure 9 shows the corresponding analytical $Q^2(z,x)$ and $v_d(t_0,x_0)$. The geometrical spreading is significant at the lower-right corner of the domain, which translates to the cost at approximately the same location in Figure 10. We use analytical Dix velocity as the input in the inversion. Starting from the Dix-inverted model and after three linearization updates, E decreases to relative 0.0045%. The size of triangular smoother is 8 m $\times$ 20 m. The model misfit, as demonstrated in Figure 11, is also improved.

Spiral model

Figure 12 shows a synthetic model borrowed from Cameron et al. (2008). The Dix inversion recovers the shallow part of the model but deteriorates quickly as geometrical spreading of image rays grows in the deeper section.

As a simple verification for the linearization process, we add a small positive velocity perturbation at location $(1,3)$ km to the synthetic model. Comparisons between the exact and linearly predicted attributes are illustrated in Figures 13, 14 and 15. In accordance with forward modeling, where we solve firstly t_0, then x_0, and finally f, the linearization (see Appendix B) is carried out following the same sequence. First, Figure 13 justifies our upwind finite-differences implementation of the linearized eikonal equation. The positive perturbation in v in Figure 12 causes t_0 to decrease in a narrow downwind region. Next, the area affected by the perturbation in Figure 14 is wider than that in Figure 13. It also has both positive and negative amplitudes. These phenomenon are physical because image rays should bend in opposite directions in

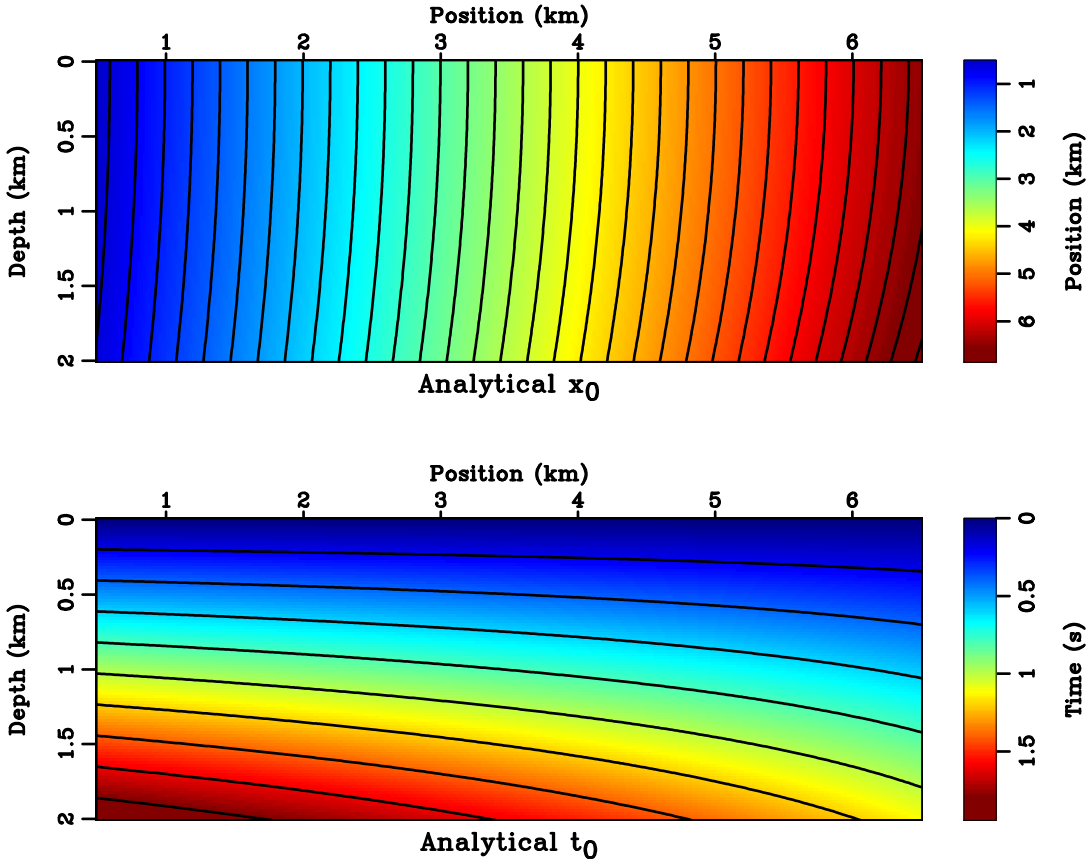

Figure 8: Analytical values of (top) t_0 and (bottom) x_0, overlaid with contour lines.

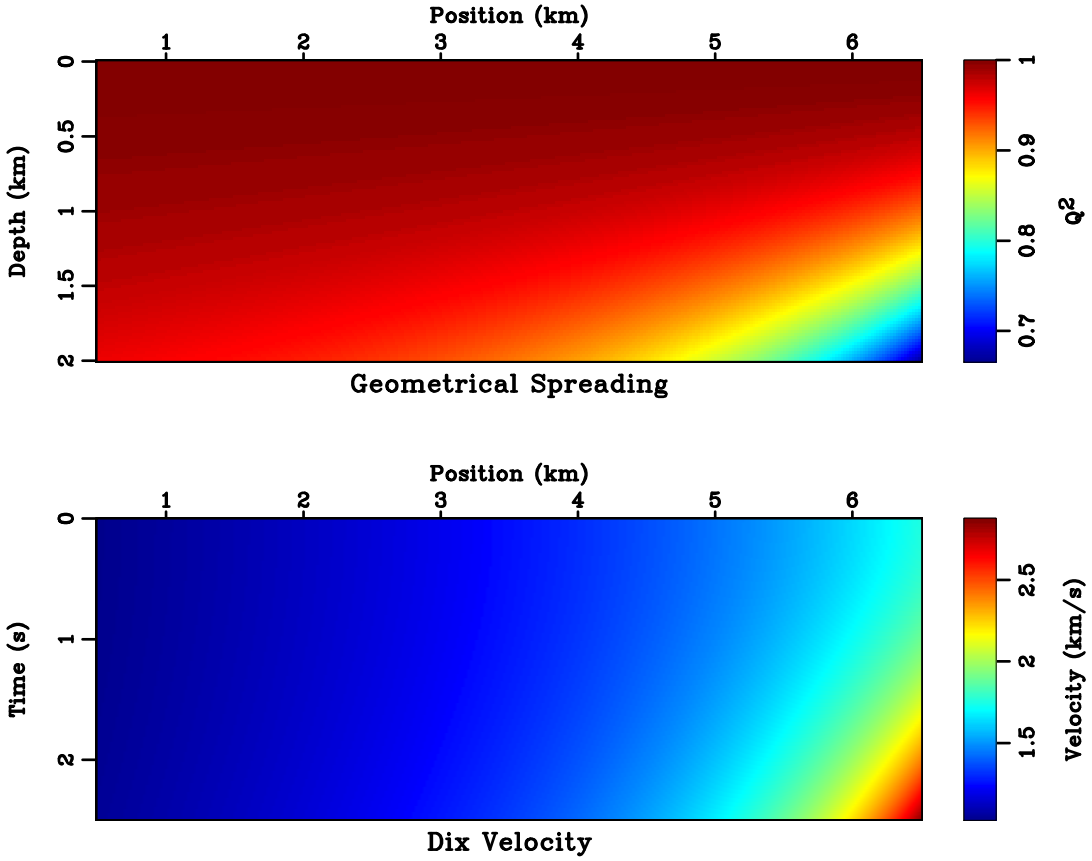

Figure 9: The (top) geometrical spreading and (bottom) Dix velocity associated with the model used in Figure 8.

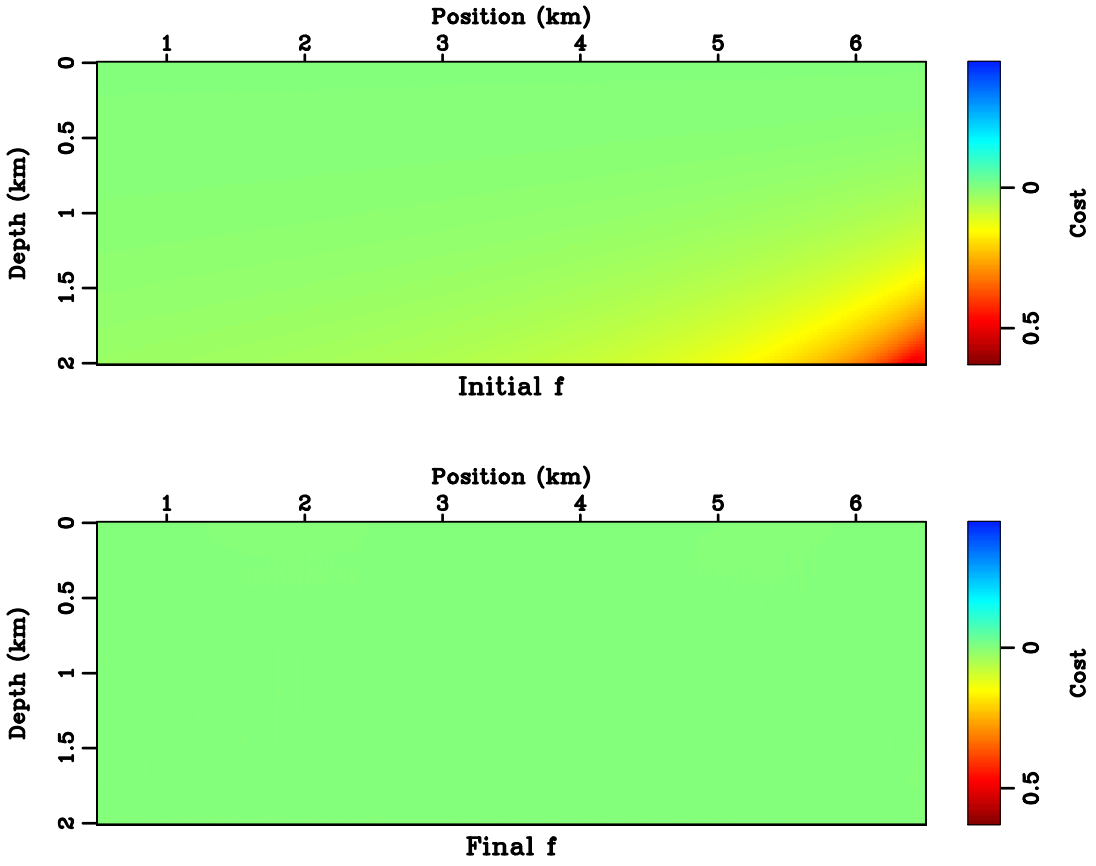

Figure 10: The cost (top) before and (bottom) after inversion. The least-squares norm of cost E is decreased from 10.431 to 0.047.

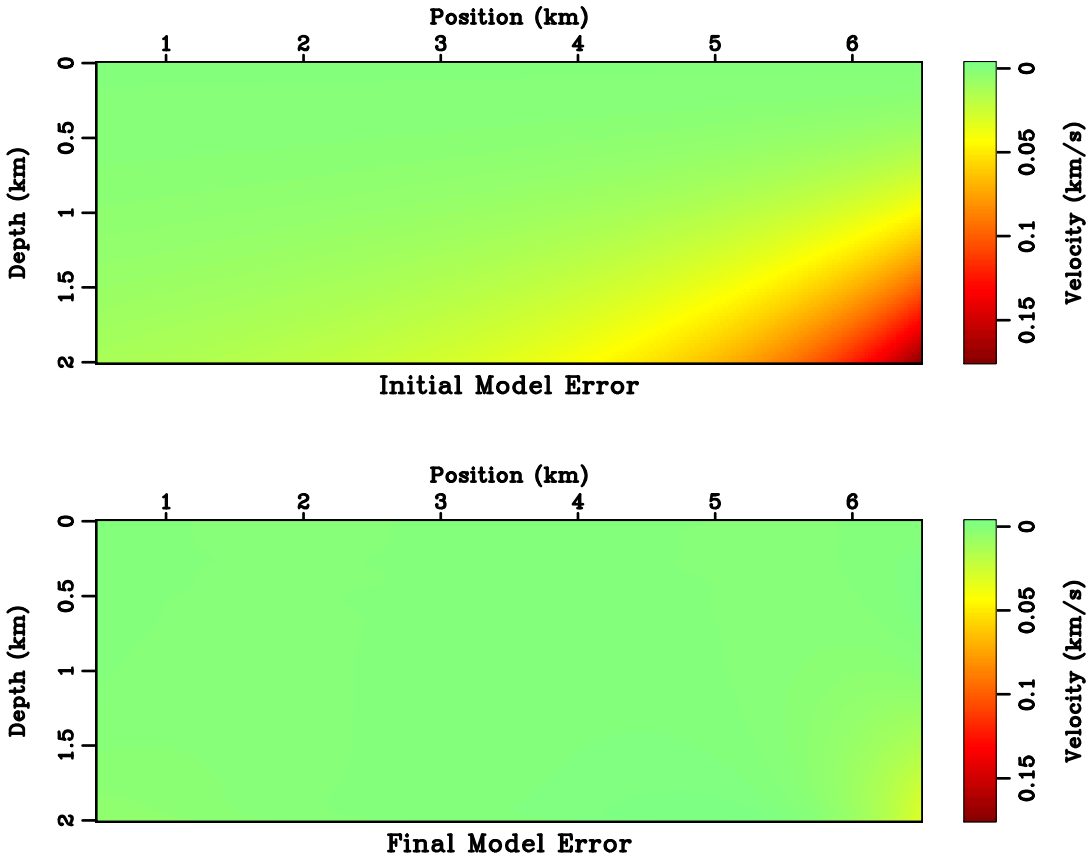

Figure 11: The difference between exact model and (top) initial model and (bottom) inverted model. The least-squares norm of model misfit is decreased from 5.0 km^2/s^2 to 0.5 km^2/s^2.

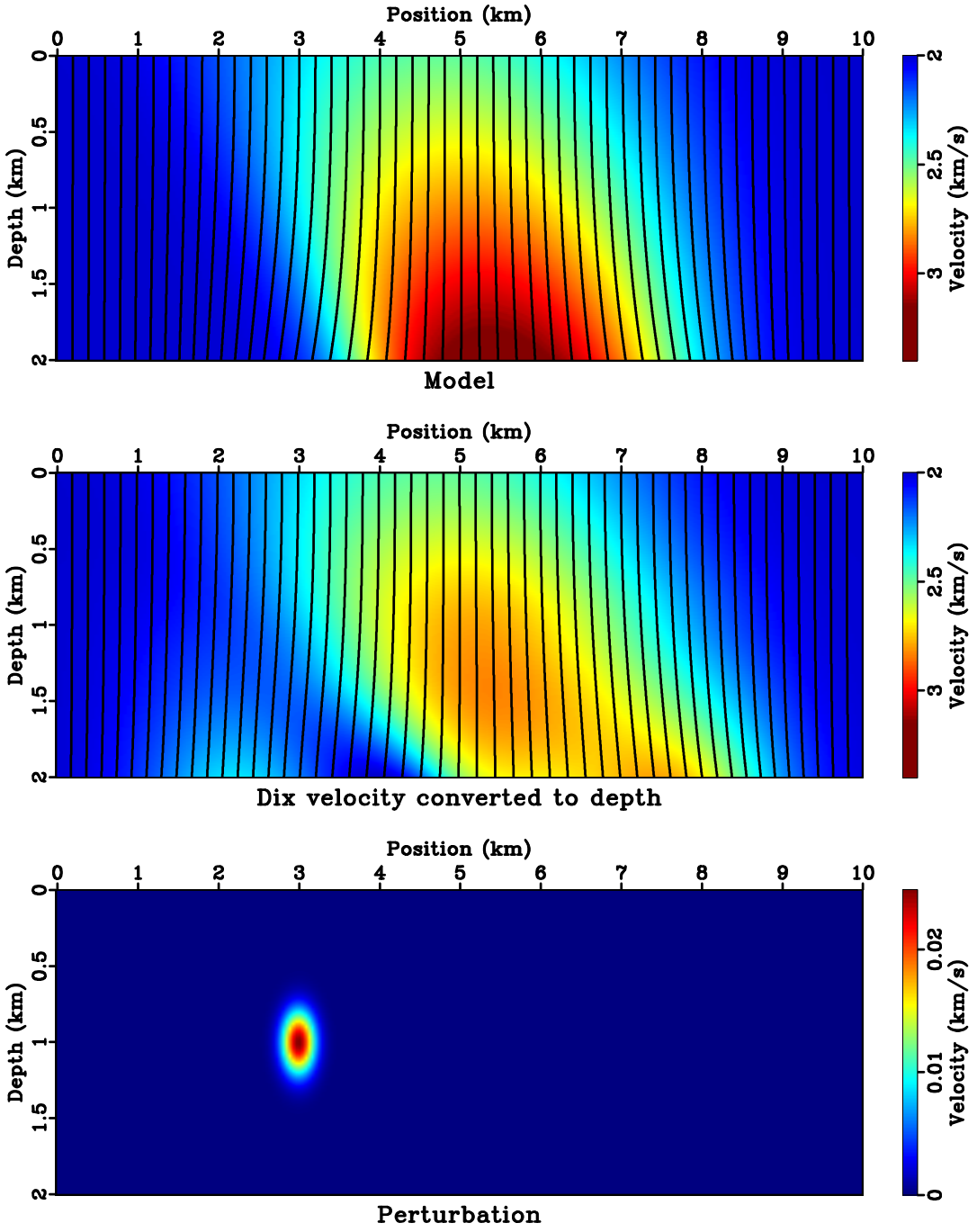

Figure 12: (Top) a synthetic model and (middle) Dix velocity converted to depth. Both overlaid with image rays. (Bottom) the model perturbation for testing linearization.

response to the perturbation. Finally, effects in cost f in Figure 15 show alternating polarities and are broader in width compared to that of dt_0 and dx_0. They indicate a complicated dependency of f on w. Note the good agreements in both shape and magnitude between exact and linearly predicted quantities in all three steps.

Because there is no analytical formula for Dix velocity in this model, we compute v_d by tracing image rays numerically in the exact model v. Also, based on Figure 12, there is no in-flow boundary other than $z = 0$. Therefore, we do not need to extend the domain as in the preceding examples. We use the Dix-inverted model as the prior model and run the inversion. It turns out that the first linearization update is sufficient for achieving the desired global minimum as shown in Figure 16.

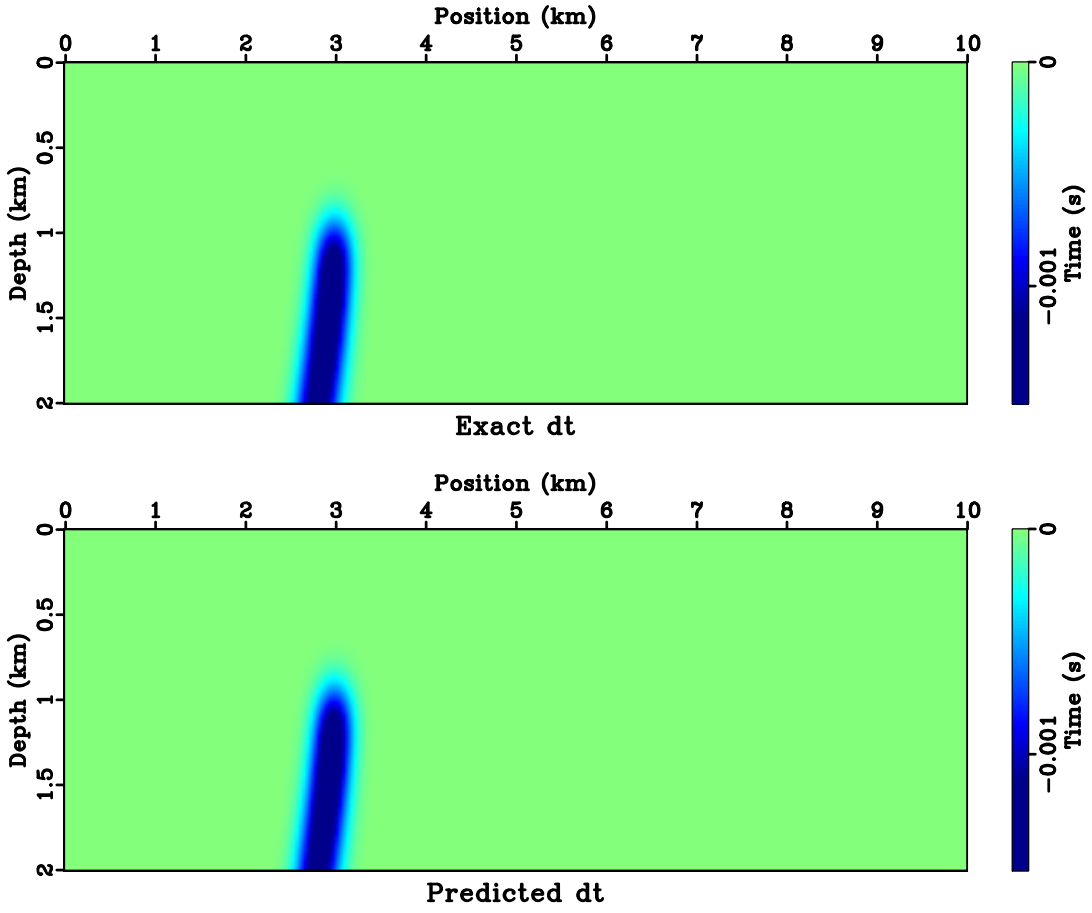

Figure 13: (Top) exact dt_0 and (bottom) linearly predicted dt_0 by equation B-4.

Field data example

The field data shown in Figure 17 is from a section of Gulf of Mexico dataset (Claerbout, 1996). We estimate v_m using the method of velocity continuation (Fomel, 2003) and convert it to v_d. Similar to the spiral model, no domain extension is needed. In

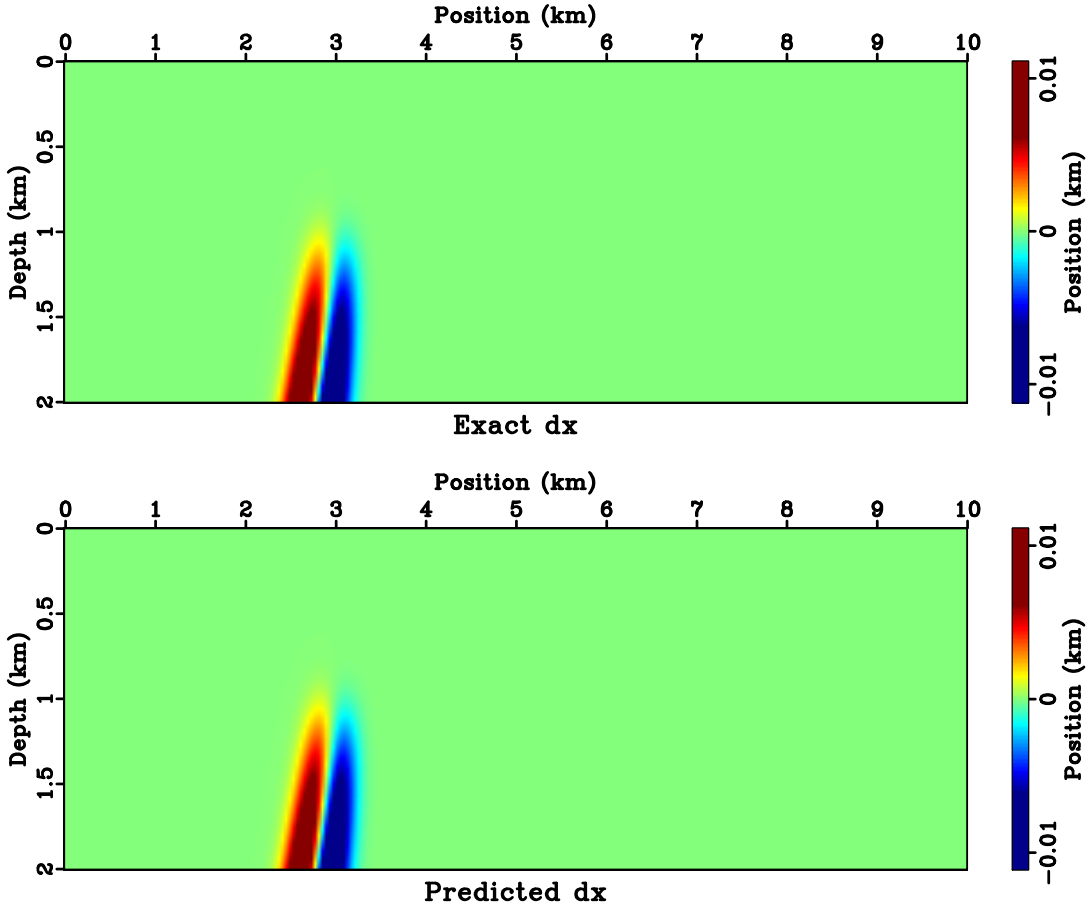

Figure 14: (Top) exact dx_0 and (bottom) linearly predicted dx_0 by equation B-3.

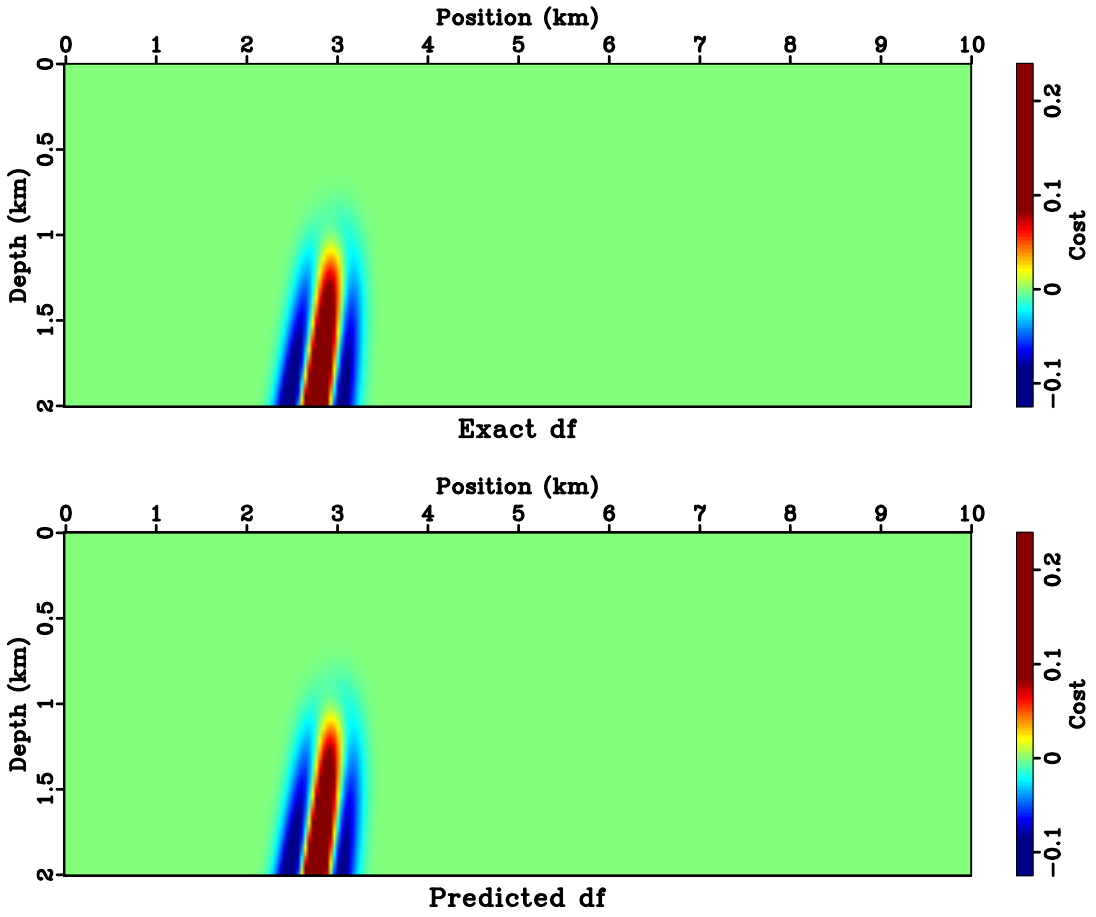

Figure 15: (Top) exact *df* and (bottom) linearly predicted *df* by equation B-5.

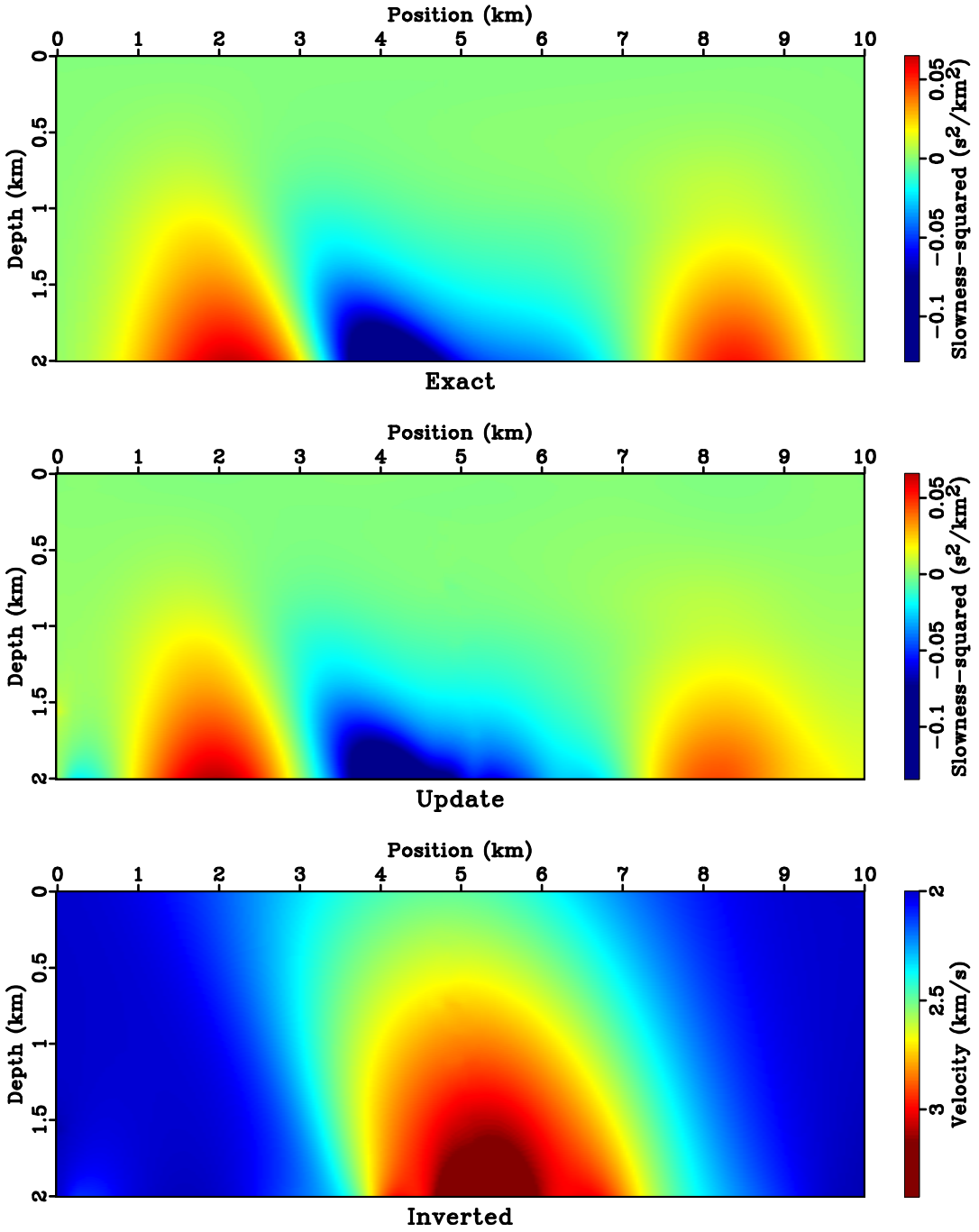

Figure 16: (Top) the exact δw and (middle) the computed δw of the first linearization step. (Bottom) the inverted interval velocity model. Compare with Figure 12.

Figure 18, the Dix-inverted prior model highly resembles the Dix velocity, because the Dix formula only scales the vertical axis from time to depth regardless of horizontal v_d variations. Figure 19 compares the cost before and after five linearization updates, with a 125 m $\times$ 335 m triangular smoother. In Figure 20, the l_2 norm of the cost, E, has a rapid decrease to relative 1.3%. Figure 21 illustrates the inverted model and interval velocity update.

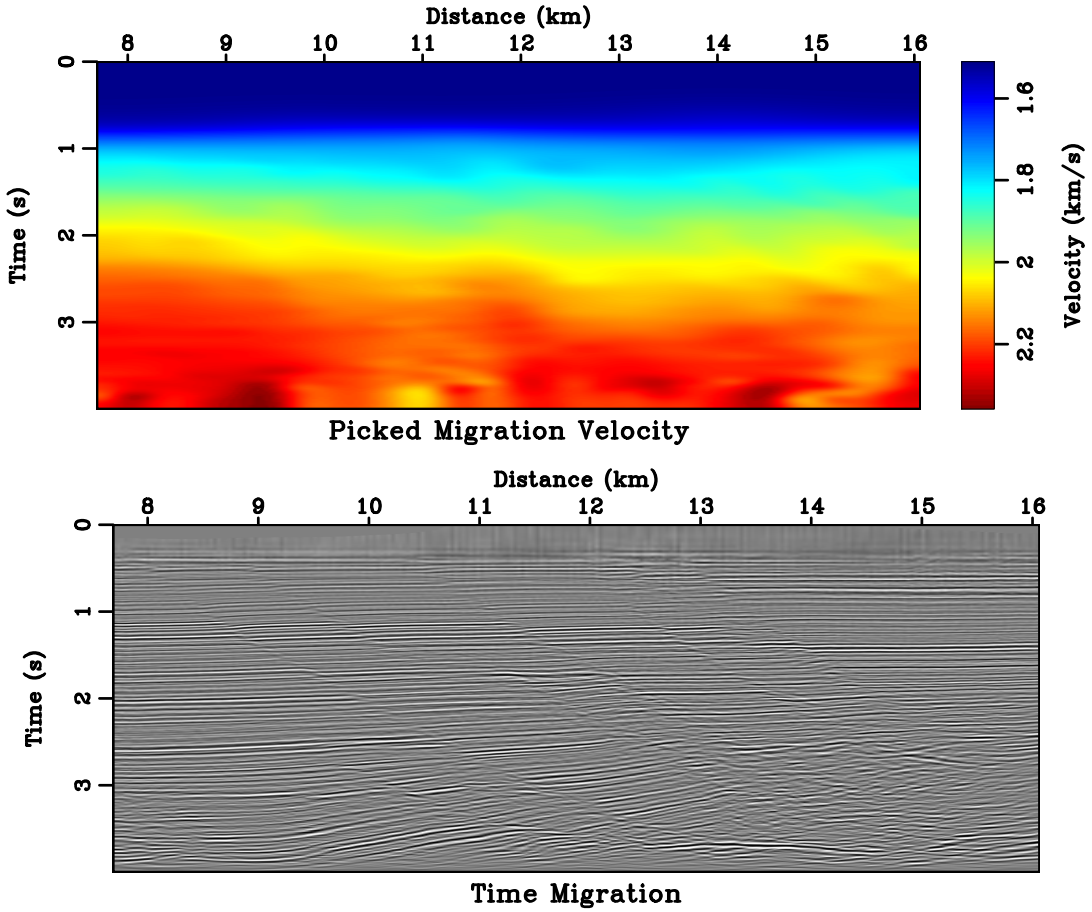

Figure 17: (Top) the estimated time-migration velocity of a section of Gulf of Mexico dataset and (bottom) the corresponding time-migrated image.

Next, we map the time-migrated image to depth using t_0 and x_0 generated during inversion. Spline interpolation (Press et al., 2007) is used during the coordinate mapping. We also migrate the prestack data by Kirchhoff depth migration (Li and Fomel, 2013) (PSDM). Figure 22 compares the time-mapped image and PSDM image of the inverted model. A good agreement between these two images justifies that time-to-depth conversion has effectively unravelled the distorted time coordinate. Figure 23 compares PSDM images of the prior and inverted models. The velocity update in Figure 21 results in not only changes in structural dips (for example at $(3, 12)$ km) but also improved reflector continuity (for example at $(3.7, 11)$ km). Moreover, the Kirchhoff migration outputs surface offset common-image gathers. We choose two

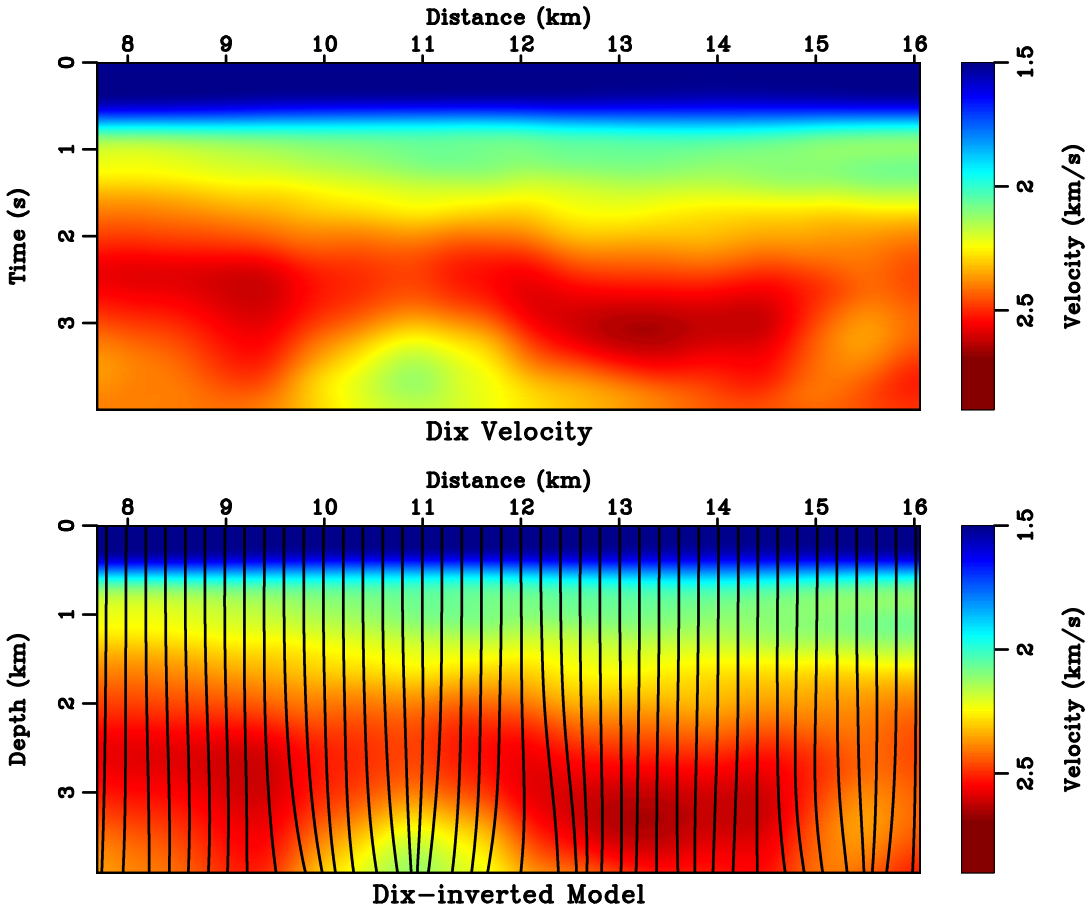

Figure 18: (Top) the Dix velocity converted from v_m in Figure 17 and (bottom) the Dix-inverted prior model for inversion, overlaid with image rays.

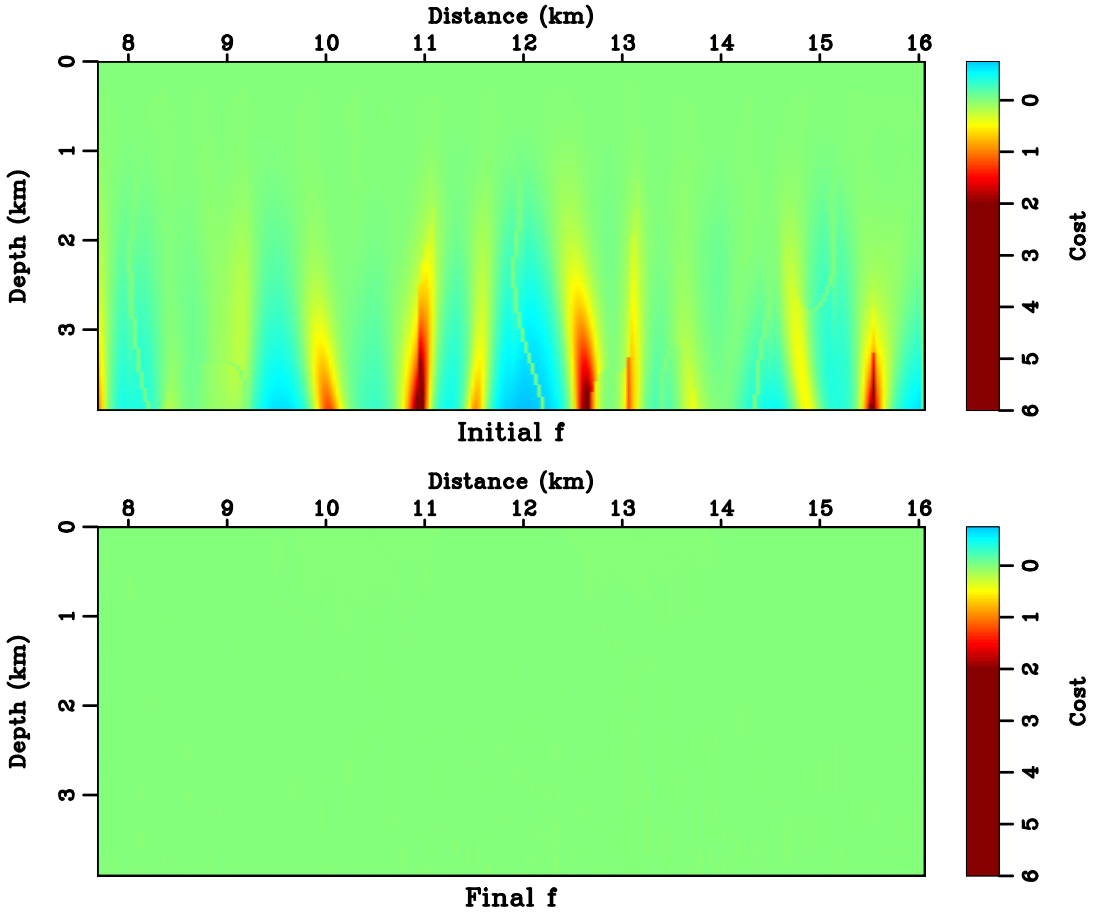

Figure 19: The cost of (top) prior model ($E = 140.25$) and (bottom) inverted model ($E = 1.81$).

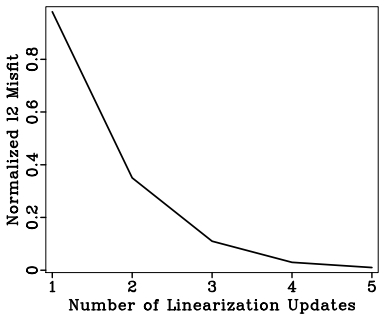

Figure 20: Convergence history of the proposed optimization-based time-to-depth conversion.

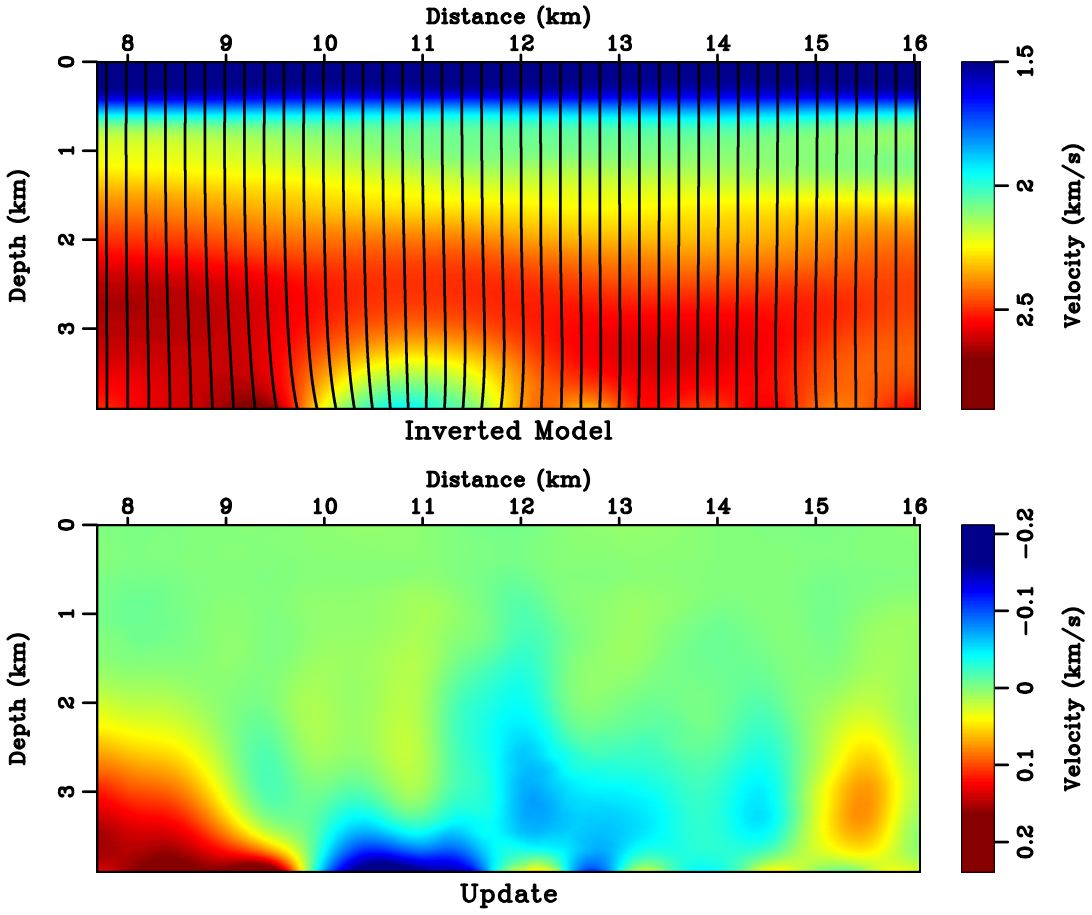

Figure 21: (Top) the inverted model, overlaid with image rays, and (bottom) its difference from the prior model in Figure 18.

midpoint locations, $x = 11$ km and $x = 12$ km, and show their common-image gathers in Figure 24. In deeper sections, flat dashed lines are overlaid as references for the flatness of gathers. The two common-image gathers of prior model appear curved in opposite directions. After time-to-depth conversion, both gathers get flattened across the whole offset range, verifying a correct velocity update.

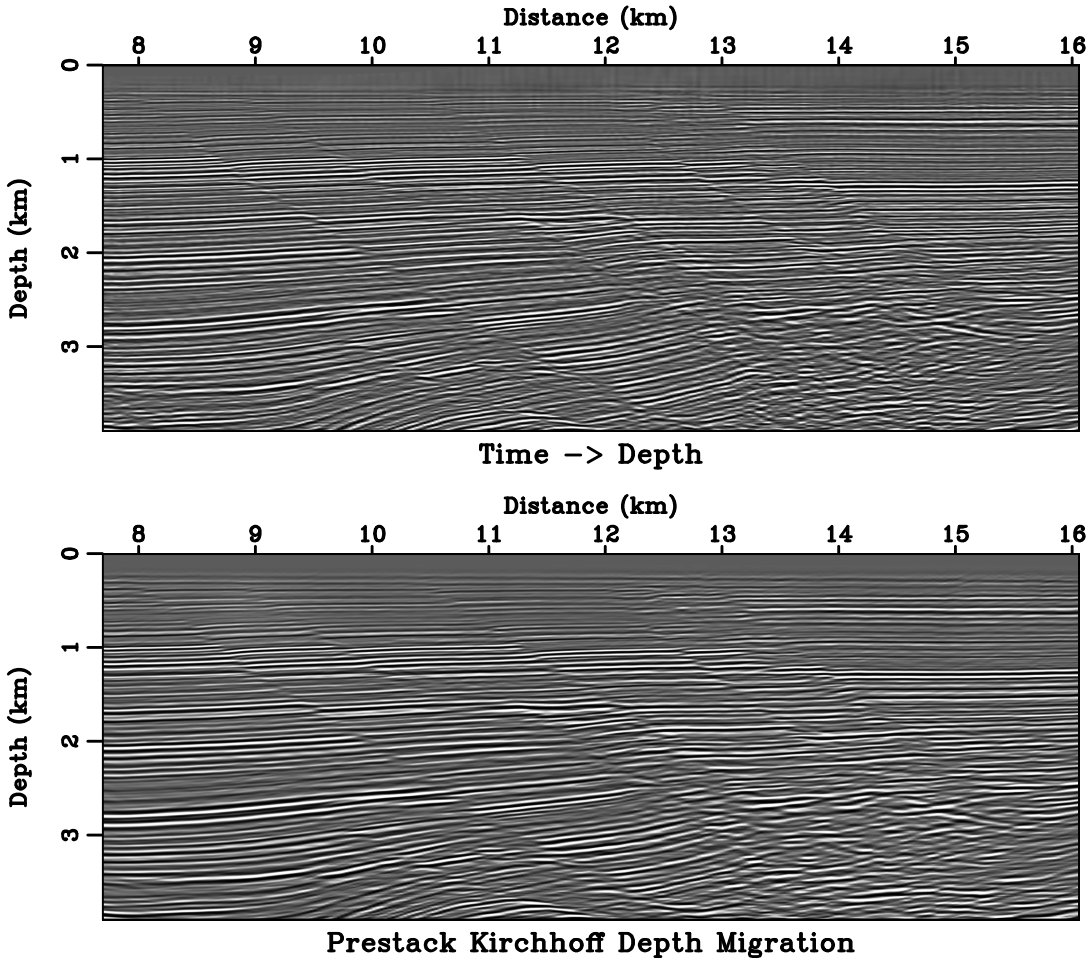

Figure 22: (Top) the time-migrated image in Figure 17 is mapped to depth using products of the time-to-depth conversion. (Bottom) PSDM image using inverted model in Figure 21.

DISCUSSION

Note that in our method the inversion is applied directly for slowness-squared $\mathbf{w}$ (and thus velocity), and the update $\delta\mathbf{w}$ will incorporate dependency of velocities throughout the domain, as physically honored by image rays. Previous methods (Cameron et al., 2007, 2008; Iversen and Tygel, 2008) that rely on time-stepping in t_0 account for such dependencies only locally. Moreover, regularization provides a

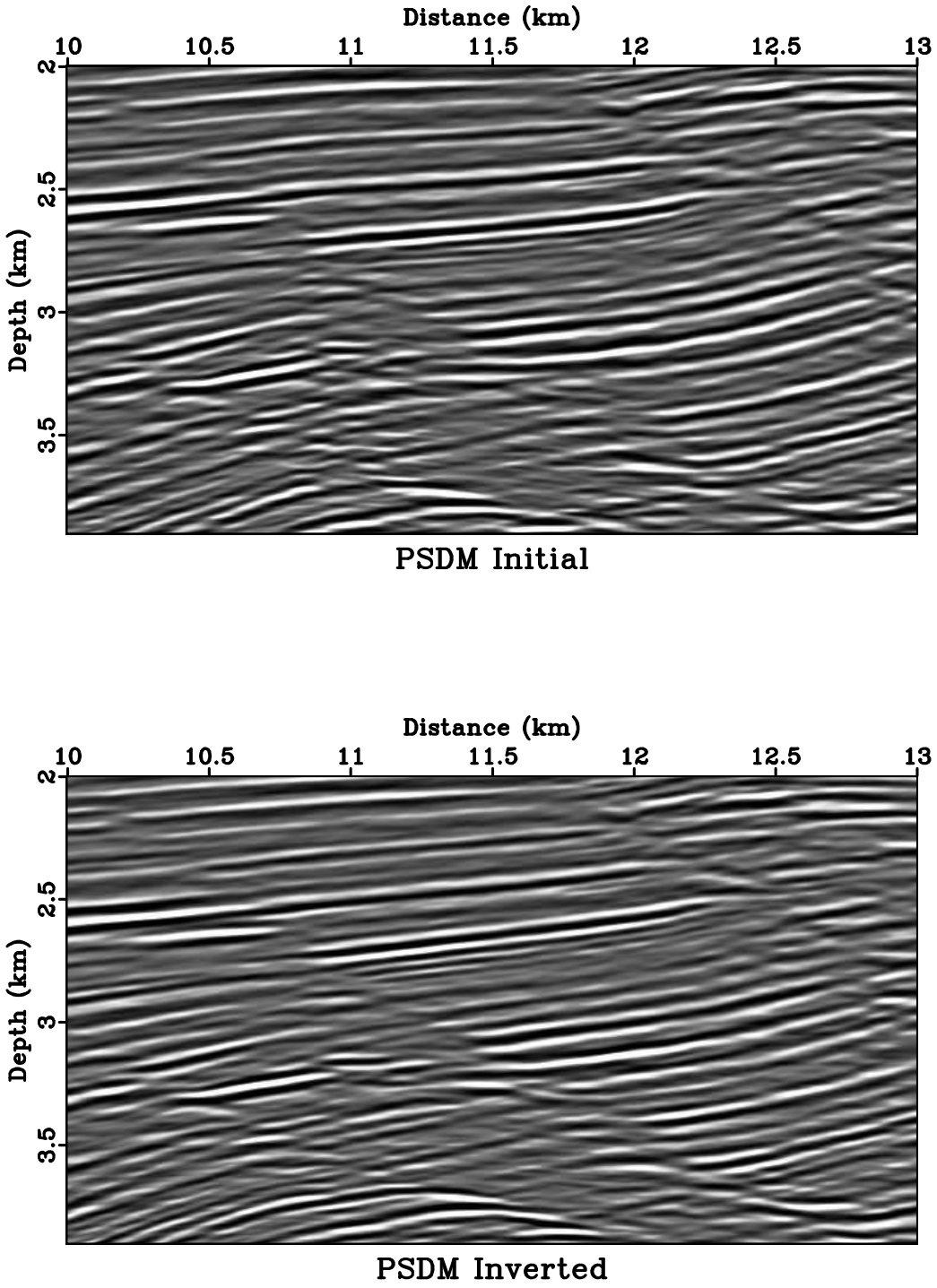

Figure 23: PSDM images of (top) the prior model and (bottom) the inverted model. Both images are plotted for the same central deep part.

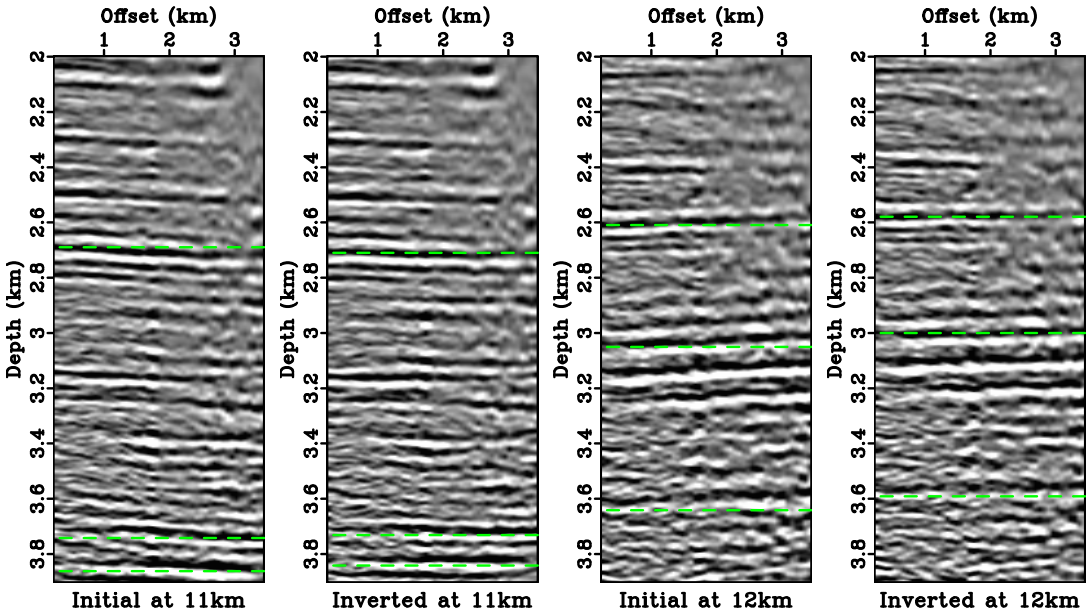

Figure 24: The surface offset common-image gathers of prior and inverted models.

convenient and effective way of handling ill-posedness of the underlying PDEs. For these reasons, the proposed method should be numerically robust compared to the previous approaches.

A 3-D extension of the proposed method is straightforward. Instead of a scalar x_0 we need to handle both inline and crossline coordinates $\mathbf{x_0} = (x_0, y_0)$. Consequently, the geometrical spreading in 3-D becomes a matrix $\mathbf{Q}$, whose determinant is related to the generalized Dix velocity $v_d(t_0, \mathbf{x_0})$ and interval velocity $v(z, \mathbf{x})$ (Cameron et al., 2007). Starting from this relationship, an iterative time-to-depth conversion can be established by following procedures similar to the ones described in this paper.

The main limitation of our approach is the failure of underlying theory at caustics, which in turn limits either the depth or the extent of lateral velocity variation of the model. A possible solution is to divide the original domain into several depth intervals, then apply velocity estimation and redatuming from one interval to another recursively (Bevc, 1997; Li and Fomel, 2013). By doing so, image-ray crossing may not develop within each interval thanks to a limited depth.

Another issue is the handling of in-flow boundaries other than the earth surface. In the synthetic examples, we avoided this problem by limiting the interval velocity model within image ray coverage. Alternatively, we could pad the input v_d laterally. The padding should simply replicate the original boundaries. By doing so, image rays at the new left and right boundaries must run straightly downward as the media there are of $v(z)$ type. Although we could not expect the inversion to fix the in-flow boundary, the resulting errors should be local around that boundary.

Finally, in our approach time-migration velocity not only determines the prior

model but also drives the inversion. Consequently, errors in time-migration velocity have a direct influence on the accuracy of inverted model. Note that usually the picking of time-migration velocity is carried out with certain smoothing. Combined with regularization in the time-to-depth conversion, the resulting interval velocity model may contain limited fine-scale features and high velocity contrasts. In this regard, we suggest our method as an efficient estimation of an initial guess for subsequent depth-imaging velocity model refinements.

CONCLUSIONS

We have introduced a novel nonlinear inversion formulation for time-to-depth velocity conversion and coordinate mapping, which involves iterative least-squares optimization constrained by a system of partial differential equations. We turn one of the governing equations that relates seismic velocity to geometrical spreading of image rays into a cost function, and linearize the other two equations: the eikonal equation and the orthogonality condition. Regularization provides extra constraints during inversion. The proposed method appears to be robust and the inversion in practice converges fast.

ACKNOWLEDGMENTS

We are grateful to Tijmen Jan Moser, Alexey Stovas, Anton Duchkov, and two anonymous reviewers for their valuable comments and suggestions. We thank BGP International for partial financial support of this research. We also thank Alexander Klokov, Alexander Vladimirsky and Changlong Wang for helpful discussions.

APPENDIX A: ILL-POSEDNESS OF THE TIME-TO-DEPTH CONVERSION PROBLEM

Let us consider the problem of solving for $z(t_0, x_0)$ and $x(t_0, x_0)$ instead of $t_0(z, x)$ and $x_0(z, x)$ by recasting equations 5, 6 and 7 in the time coordinates:

$$\left(\frac{\partial x}{\partial x_0}\right)^2 + \left(\frac{\partial z}{\partial x_0}\right)^2 = \frac{v^2(z(t_0,x_0),x(t_0,x_0))}{v_d^2(t_0,x_0)} \;, \tag{A-1}$$

$$\left(\frac{\partial x}{\partial t_0}\right)^2 + \left(\frac{\partial z}{\partial t_0}\right)^2 = v^2(z(t_0,x_0),x(t_0,x_0)) \;, \tag{A-2}$$

$$\frac{\partial x}{\partial x_0}\frac{\partial x}{\partial t_0} + \frac{\partial z}{\partial x_0}\frac{\partial z}{\partial t_0} = 0 \;. \tag{A-3}$$

The corresponding boundary conditions are

$$\left\{ \begin{array}{rcl} z(0,x_0) &=& 0 \;, \\ x(0,x_0) &=& x_0 \;. \end{array} \right. \tag{A-4}$$

From equation A-3

$$\frac{\partial x}{\partial t_0} = -\frac{\partial z}{\partial x_0}\frac{\partial z}{\partial t_0}\Big/\frac{\partial x}{\partial x_0} \ . \tag{A-5}$$

Substituting equation A-5 into equation A-2 and combining with equation A-1 produces

$$\frac{\partial z}{\partial t_0} = v_d \frac{\partial x}{\partial x_0} \ ; \tag{A-6}$$

$$\frac{\partial x}{\partial t_0} = -v_d \frac{\partial z}{\partial x_0} \ , \tag{A-7}$$

where we assume that both $\partial z/\partial t_0$ and $\partial x/\partial x_0$ remain positive and there is no caustics.

On the first glance, equations A-6 and A-7 seem suitable for numerically extrapolating $x(t_0, x_0)$ and $z(t_0, x_0)$ in t_0 direction using the boundary conditions A-4. After such an extrapolation, one would be able to reconstruct $v(t_0, x_0)$ from equation A-2 and thus solve the original problem. However, by further decoupling the system using the equivalence of the second-order mixed derivatives, we discover that the underlying PDEs are elliptic. For instance, applying $\partial/\partial x_0$ to both sides of equation A-7 results in

$$\frac{\partial^2 x}{\partial t_0 \partial x_0} = -\frac{\partial}{\partial x_0}\left(v_d \frac{\partial z}{\partial x_0}\right) \ . \tag{A-8}$$

Meanwhile, dividing by v_d and applying $\partial/\partial t_0$ to both sides of equation A-6 leads to

$$\frac{\partial}{\partial t_0}\left(\frac{1}{v_d}\frac{\partial z}{\partial t_0}\right) = \frac{\partial^2 x}{\partial x_0 \partial t_0} \ . \tag{A-9}$$

Comparing equations A-8 and A-9, we find

$$\frac{\partial}{\partial x_0}\left(v_d \frac{\partial z}{\partial x_0}\right) + \frac{\partial}{\partial t_0}\left(\frac{1}{v_d}\frac{\partial z}{\partial t_0}\right) = 0 \ . \tag{A-10}$$

Analogously,

$$\frac{\partial}{\partial x_0}\left(v_d \frac{\partial x}{\partial x_0}\right) + \frac{\partial}{\partial t_0}\left(\frac{1}{v_d}\frac{\partial x}{\partial t_0}\right) = 0 \ . \tag{A-11}$$

Solving elliptic equations A-10 and A-11 with the Cauchy-type boundary conditions A-4 is an ill-posed problem (Evans, 2010). A different formulation, leading to a non-linear elliptic PDE, was previously discussed by Cameron et al. (2009).

APPENDIX B: THE FRÉCHET DERIVATIVE OPERATOR

We continue the derivation of the Fréchet derivative matrix from equation 12. Using the same notations as introduced in equation 10, after discretization equation 12

becomes

$$\mathbf{J} \equiv \frac{\partial \mathbf{f}}{\partial \mathbf{w}} = 2\,\mathbf{L}_{x_0}\,\frac{\partial \mathbf{x_0}}{\partial \mathbf{w}} - 2\,\mathrm{diag}(\mathbf{v_d} \star \mathbf{w})\,\frac{\partial \mathbf{v_d}}{\partial \mathbf{w}} - \mathrm{diag}(\mathbf{v_d} \star \mathbf{v_d})\ . \tag{B-1}$$

Because v_d is in time-domain (t_0, x_0), we need to apply the chain-rule for its derivative with respect to w, i.e.,

$$\frac{\partial \mathbf{v_d}}{\partial \mathbf{w}} = \frac{\partial \mathbf{v_d}}{\partial \mathbf{t_0}}\,\frac{\partial \mathbf{t_0}}{\partial \mathbf{w}} + \frac{\partial \mathbf{v_d}}{\partial \mathbf{x_0}}\,\frac{\partial \mathbf{x_0}}{\partial \mathbf{w}}\ , \tag{B-2}$$

where $\mathbf{t_0}$ is the discretized column vector of $t_0(z, x)$. According to equation 7 and after denoting another matrix operator $\mathbf{L}_{t_0} = \nabla \mathbf{t_0} \cdot \nabla$, we find

$$\frac{\partial \mathbf{x_0}}{\partial \mathbf{w}} = -(\nabla \mathbf{t_0} \cdot \nabla)^{-1}(\nabla \mathbf{x_0} \cdot \nabla)\,\frac{\partial \mathbf{t_0}}{\partial \mathbf{w}} \equiv -\mathbf{L}_{t_0}^{-1}\mathbf{L}_{x_0}\,\frac{\partial \mathbf{t_0}}{\partial \mathbf{w}}\ . \tag{B-3}$$

Another differentiation of equation 6 leads to

$$\frac{\partial \mathbf{t_0}}{\partial \mathbf{w}} = \frac{1}{2}(\nabla \mathbf{t_0} \cdot \nabla)^{-1} \equiv \frac{1}{2}\mathbf{L}_{t_0}^{-1}\ . \tag{B-4}$$

Finally, by inserting equations B-2 through B-4 into B-1, we complete the derivation of the Fréchet derivative matrix:

$$\begin{aligned} \mathbf{J} &= -\mathbf{L}_{x_0}\mathbf{L}_{t_0}^{-1}\mathbf{L}_{x_0}\mathbf{L}_{t_0}^{-1} - \mathrm{diag}(\mathbf{v_d} \star \mathbf{w})\frac{\partial \mathbf{v_d}}{\partial \mathbf{t_0}}\mathbf{L}_{t_0}^{-1} \\ &+ \mathrm{diag}(\mathbf{v_d} \star \mathbf{w})\frac{\partial \mathbf{v_d}}{\partial \mathbf{x_0}}\mathbf{L}_{t_0}^{-1}\mathbf{L}_{x_0}\mathbf{L}_{t_0}^{-1} - \mathrm{diag}(\mathbf{v_d} \star \mathbf{v_d})\ . \end{aligned} \tag{B-5}$$

APPENDIX C: ANALYTICAL EXPRESSIONS FOR THE CONSTANT VELOCITY GRADIENT MEDIUM

In order to derive the time-to-depth conversion analytically, we first trace image rays in the depth coordinate for $z(t_0, x_0)$ and $x(t_0, x_0)$. Then we carry out a direct inversion to find $t_0(z, x)$ and $x_0(z, x)$. The Dix velocity can be obtained at last following equations 3 and 4.

Continuing from equation 15, we write the velocity in a coordinate relative to the image ray

$$v(z, x) = v_0 + g_z z + g_x x = \tilde{v}_0 + \mathbf{g} \cdot (\mathbf{x} - \mathbf{x_0})\ , \tag{C-1}$$

where $\mathbf{g} = [g_z, g_x]^T$ and $\tilde{v}_0 = v_0 + g_x x_0$. At the starting point, image ray satisfies

$$\left\{ \begin{array}{lcl} \mathbf{x_0} &=& [0, x_0]^T\ , \\ \mathbf{p_0} &=& [\tilde{v}_0^{-1}, 0]^T\ , \\ t_0 &=& t\ . \end{array} \right. \tag{C-2}$$

Here we denote ray parameter $\mathbf{p} = \nabla t$ and $\mathbf{p_0}$ is the ray parameter at source. The Hamiltonian for ray tracing reads $H(\mathbf{x}, \mathbf{p}) = \mathbf{p} \cdot \mathbf{p} - v^{-2} \equiv 0$. The corresponding ray tracing system is (Červený, 2001):

$$\left\{ \begin{array}{lcl} d\mathbf{x}/d\xi &=& \mathbf{p}v^3 \ , \\ d\mathbf{p}/d\xi &=& -\nabla v \ , \\ dt/d\xi &=& \nabla t \cdot d\mathbf{x}/d\xi = \mathbf{p} \cdot \mathbf{p}v^3 = v \ . \end{array} \right. \tag{C-3}$$

Equation C-1 indicates $\nabla v = \mathbf{g}$, which means $d\mathbf{p}/d\xi$ can be integrated analytically and provides

$$\mathbf{p} = \mathbf{p_0} - \mathbf{g}\xi \ . \tag{C-4}$$

From the eikonal equation and considering $\mathbf{p_0} \cdot \mathbf{p_0} = \tilde{v}_0^{-2}$ and $g = |\mathbf{g}| = \sqrt{g_z^2 + g_x^2}$, we have

$$v = \frac{1}{\sqrt{\mathbf{p} \cdot \mathbf{p}}} = \left(\tilde{v}_0^{-2} - 2\mathbf{p_0} \cdot \mathbf{g}\xi + g^2\xi^2 \right)^{-\frac{1}{2}} \ . \tag{C-5}$$

Integrating equation C-5 over ξ gives

$$t = \frac{1}{g} \text{arccosh} \left(1 + \frac{g^2\xi^2}{\tilde{v}_0^{-2} + v^{-1}\tilde{v}_0^{-1} - \mathbf{p_0} \cdot \mathbf{g}\xi} \right) \ . \tag{C-6}$$

Meanwhile, combining equations C-1 and C-3, we find $d\mathbf{p}/d\xi \cdot (\mathbf{x} - \mathbf{x_0}) + d\mathbf{x}/d\xi \cdot \mathbf{p} = \tilde{v}_0$, i.e., $\mathbf{p} \cdot (\mathbf{x} - \mathbf{x_0}) = \tilde{v}_0\xi$. Suppose

$$\mathbf{x} - \mathbf{x_0} = \alpha\mathbf{p_0} + \beta\mathbf{g} \tag{C-7}$$

then

$$\left\{ \begin{array}{lcl} \mathbf{g} \cdot (\mathbf{x} - \mathbf{x_0}) &=& \alpha\mathbf{p_0} \cdot \mathbf{g} + \beta g^2 = v - \tilde{v}_0 \ , \\ \mathbf{p_0} \cdot (\mathbf{x} - \mathbf{x_0}) &=& \alpha\tilde{v}_0^{-2} + \beta\mathbf{p_0} \cdot \mathbf{g} = \tilde{v}_0\xi + (v - \tilde{v}_0)\xi = v\xi \ . \end{array} \right. \tag{C-8}$$

Solving equation C-8 provides $\alpha(\xi, v)$ and $\beta(\xi, v)$, which after substituting into equation C-7 leads to

$$\mathbf{x} = \mathbf{x_0} + \frac{(v - \tilde{v}_0)\left[\mathbf{g} - (\mathbf{p_0} \cdot \mathbf{g})\tilde{v}_0^2\mathbf{p_0}\right] + v\tilde{v}_0^2\left[g^2\mathbf{p_0} - (\mathbf{p_0} \cdot \mathbf{g})\mathbf{g}\right]\xi}{g^2 - (\mathbf{p_0} \cdot \mathbf{g})^2\tilde{v}_0^2} \ . \tag{C-9}$$

Note equation C-2 states $\mathbf{p_0} \cdot \mathbf{g} = g_z\tilde{v}_0^{-1}$ and thus equations C-4, C-6 and C-9 can be further simplified.

To connect depth- and time-domain attributes, we first invert equation C-6 such that ξ is expressed by t_0 and x_0

$$\xi(t_0, x_0) = \frac{g_z(1 - \cosh(|gt_0|)) + g\sinh(gt_0)}{g^2\tilde{v}_0^2} \ . \tag{C-10}$$

Next, we insert equations C-5 and C-10 into C-9 in order to change its parameterization from (ξ, v) to (t_0, x_0). The result is written for the z and x components of $\mathbf{x}$ separately, as follows:

$$x(t_0, x_0) = x_0 + \frac{\tilde{v}_0 g_x(1 - \cosh(gt_0))}{g(g\cosh(gt_0) - g_z\sinh(gt_0))} \ , \tag{C-11}$$

$$z(t_0,x_0)=\frac{\tilde{v}_0\left[g_z(1-\cosh(gt_0))+g\sinh(gt_0)\right]}{g(g\cosh(gt_0)-g_z\sinh(gt_0))}\ . \tag{C-12}$$

Inverting equations C-11 and C-12 results in

$$x_0(z,x)=x+\frac{\sqrt{(v_0+g_xx)^2+g_x^2z^2}-(v_0+g_xx)}{g_x}\ , \tag{C-13}$$

$$t_0(z,x)=\frac{1}{g}\text{arccosh}\left\{\frac{g^2\left[\sqrt{(v_0+g_xx)^2+g_x^2z^2}+g_zz\right]-vg_z^2}{vg_x^2}\right\}\ . \tag{C-14}$$

In the last step, we derive the analytical formula for the Dix velocity. Note that from equation C-13 $|\nabla x_0|^2=1$, i.e., there is no geometrical spreading. The image rays are circles parallel to each other. Therefore according to equation 3 $v_d=v$ and is found by combining equations C-5 and C-10

$$v_d(t_0,x_0)=\frac{(v_0+g_xx_0)g}{g\cosh(gt_0)-g_z\sinh(gt_0)}\ . \tag{C-15}$$

The time-migration velocity v_m, on the other hand, is

$$v_m(t_0,x_0)=\frac{(v_0+g_xx_0)^2}{t_0(g\coth(gt_0)-g_z)}\ . \tag{C-16}$$

APPENDIX D: ANALYTICAL EXPRESSIONS FOR THE CONSTANT HORIZONTAL SLOWNESS-SQUARED GRADIENT MEDIUM

In this appendix, we study the following medium:

$$w(z,x)=w_0-2q_xx=w_0-2\mathbf{q}\cdot\mathbf{x}\ , \tag{D-1}$$

where $\mathbf{q}=[0,q_x]^T$.

Similarly to the constant velocity gradient medium, it is convenient to write down the ray-tracing system in the form (Červený, 2001)

$$\left\{\begin{array}{lcl} d\mathbf{x}/d\sigma &=& \mathbf{p}\ , \\ d\mathbf{p}/d\sigma &=& \nabla w/2\ , \\ dt/d\sigma &=& \nabla t\cdot d\mathbf{x}/d\sigma=\mathbf{p}\cdot\mathbf{p}\ . \end{array}\right. \tag{D-2}$$

Given equation D-1, $\nabla w=-2\mathbf{q}$ and thus $d\mathbf{p}/d\sigma=-\mathbf{q}$. After integration over σ, equation D-2 becomes

$$\left\{\begin{array}{lcl} \mathbf{x} &=& \mathbf{x_0}+\mathbf{p_0}\sigma-\mathbf{q}\sigma^2/2\ , \\ \mathbf{p} &=& \mathbf{p_0}-\mathbf{q}\sigma\ , \\ t &=& |\mathbf{p_0}|^2\sigma-\mathbf{p_0}\cdot\mathbf{q}\sigma^2+|\mathbf{q}|^2\sigma^3/3\ . \end{array}\right. \tag{D-3}$$

For a particular image ray

$$\begin{cases} \mathbf{x_0} &= [0, x_0]^T \ , \\ \mathbf{p_0} &= [\sqrt{w_0 - 2q_x x_0}, 0]^T \ , \\ t_0 &= t \ , \end{cases} \tag{D-4}$$

the equation for $\mathbf{x}$ in D-3 simplifies to

$$\begin{cases} x = x_0 - q_x \sigma^2/2 \ , \\ z = \sigma \sqrt{w_0 - 2q_x x_0} \ . \end{cases} \tag{D-5}$$

Solving equation D-5 for σ as a function of z and x

$$\sigma(z,x) = \left[\frac{(w_0 - 2q_x x) - \sqrt{(w_0 - 2q_x x)^2 - 4q_x^2 z^2}}{2q_x^2} \right]^{\frac{1}{2}} \ . \tag{D-6}$$

Combining equations D-3 through D-6, we find

$$\begin{aligned} x_0(z,x) &= x + \frac{1}{2} q_x \sigma^2 \\ &= \frac{2w_0 x + q_x z^2}{w_0 + 2q_x x + \sqrt{(w_0 - 2q_x x)^2 - 4q_x^2 z^2}} \ , \end{aligned} \tag{D-7}$$

$$\begin{aligned} t_0(z,x) &= (w_0 - 2q_x x_0)\sigma + \frac{1}{3} q_x^2 \sigma^3 \\ &= \frac{\sqrt{2} z \left[2w_0 - 4q_x x + \sqrt{(w_0 - 2q_x x)^2 - 4q_x^2 z^2} \right]}{3 \left[w_0 - 2q_x x + \sqrt{(w_0 - 2q_x x)^2 - 4q_x^2 z^2} \right]^{\frac{1}{2}}} \ . \end{aligned} \tag{D-8}$$

According to equation 4, D-7 can give rise to the geometrical spreading:

$$Q^2(z,x) = \frac{2[(w_0 - 2q_x x)^2 - 4q_x^2 z^2]}{(w_0 - 2q_x x) \left[w_0 - 2q_x x + \sqrt{(w_0 - 2q_x x)^2 - 4q_x^2 z^2} \right]} \ . \tag{D-9}$$

It is more convenient to express equations D-1 and D-9 in σ and x_0 instead of directly in t_0 and x_0:

$$w(\sigma, x_0) = w_0 - 2q_x x_0 + q_x^2 \sigma^2 \ , \tag{D-10}$$

$$Q^2(\sigma, x_0) = 1 + q_x^2 \sigma^2 \left(\frac{1}{w_0 - 2q_x x_0} - \frac{4}{w_0 - 2q_x x_0 + q_x^2 \sigma^2} \right) \ , \tag{D-11}$$

where we must resolve $\sigma = \sigma(t_0, x_0)$. This is done by revisiting equation D-8. For given t_0 and x_0, σ is the root of a depressed cubic function of the following form:

$$\sigma^3 + \frac{3(w_0 - 2q_x x_0)}{q_x^2} \sigma - \frac{3}{q_x^2} t_0 = 0 \ . \tag{D-12}$$

After some algebraic manipulations, we find

$$\begin{aligned}\sigma(t_0,x_0) &= \left[\frac{3t_0+\sqrt{9t_0^2+4(w_0-2q_xx_0)^3/q_x^2}}{2q_x^2}\right]^{\frac{1}{3}} \\ &- \frac{w_0-2q_xx_0}{q_x}\left[\frac{2}{3q_xt_0+\sqrt{9q_x^2t_0^2+4(w_0-2q_xx_0)^3}}\right]^{\frac{1}{3}} . \end{aligned} \quad \text{(D-13)}$$

Finally, inserting equations D-10 and D-11 into equation 3 results in the Dix velocity:

$$v_d(t_0,x_0)=\frac{\sqrt{w_0-2q_xx_0}}{w_0-2q_xx_0-q_x^2\sigma^2} . \quad \text{(D-14)}$$

REFERENCES

Bartel, D., M. Busby, J. Nealon, and J. Zaske, 2006, Time to depth conversion and uncertainty assessment using average velocity modeling: 66th Annual International Meetings, SEG Expanded Abstracts, 2166–2170.

Bevc, D., 1997, Imaging complex structures with semirecursive Kirchhoff migration: Geophysics, **62**, 577–588.

Bevc, D., J. L. Black, and G. Palacharla, 1995, Plumes: Response of time migration to lateral velocity variation: Geophysics, **60**, 1118–1127.

Bishop, T. N., K. P. Bube, R. T. Cutler, R. T. Langan, P. L. Love, J. R. Resnick, R. T. Shuey, D. A. Spindler, and H. W. Wyld, 1985, Tomographic determination of velocity and depth in laterally varying media: Geophysics, **50**, 903–923.

Björck, A., 1996, Numerical methods for least squares problems: SIAM.

Black, J. L., and M. A. Brzostowski, 1994, Systematics of time migration errors: Geophysics, **59**, 1419–1434.

Cameron, M., S. Fomel, and J. Sethian, 2007, Seismic velocity estimation from time migration: Inverse Problems, **23**, 1329–1369.

———, 2008, Time-to-depth conversion and seismic velocity estimation using time-migration velocity: Geophysics, **73**, no. 5, VE205–VE210.

———, 2009, Analysis and algorithms for a regularized Cauchy problem arising from a nonlinear elliptic PDE for seismic velocity estimation: Journal of Computational Physics, **228**, 7388–7411.

Chapman, C., 2004, Fundamentals of seismic wave propagation: Cambridge University Press.

Claerbout, J. F., 1996, Basic earth imaging: http://sepwww.stanford.edu/sep/prof/bei10.2008.pdf.

Dix, C. H., 1955, Seismic velocities from surface measurements: Geophysics, **20**, 68–86.

Engl, H. W., M. Hanke, and A. Neubauer, 1996, Regularization of inverse problems: Kluwer Academic Publishers.

Evans, L. C., 2010, Partial differential equations: American Mathematical Society.

Fomel, S., 2003, Time-migration velocity analysis by velocity continuation: Geophysics, **68**, 1662–1672.

———, 2007, Shaping regularization in geophysical estimation problems: Geophysics, **72**, no. 2, R29–R36.

Franklin, J. B., and J. M. Harris, 2001, A fast marching level set method for monotonically advancing fronts: Journal of Computational Acoustics, **9**, 1095–1109.

Haddon, R. A. W., and P. W. Buchen, 1981, Use of Kirchhoff's formula for body wave calculations in the earth: Geophysical Journal of the Royal Astronomical Society, **67**, 587–598.

Hestenes, M. R., and E. Stiefel, 1952, Method of conjugate gradients for solving linear systems: Journal of Research of the National Bureau of Standards, **49**, 409–436.

Hubral, P., 1977, Time migration—some ray theoretical aspects: Geophysical Prospecting, **25**, 738–745.

Iversen, E., and M. Tygel, 2008, Image-ray tracing for joint 3D seismic velocity estimation and time-to-depth conversion: Geophysics, **73**, S99–S114.

Larner, K. L., L. Hatton, B. S. Gibson, and I. S. Hsu, 1981, Depth migration of imaged time sections: Geophysics, **46**, 734–750.

Li, S., and S. Fomel, 2013, Kirchhoff migration using eikonal-based computation of traveltime source-derivatives: Geophysics, **78**, no. 4, S211–S219.

Li, S., S. Fomel, and A. Vladimirsky, 2011, Improving wave-equation fidelity of Gaussian beams by solving the complex eikonal equation: 71st Annual International Meetings, SEG Expanded Abstracts, 3829–3834.

Li, S., A. Vladimirsky, and S. Fomel, 2013, First-break traveltime tomography with the double-square-root eikonal equation: Geophysics, **78**, no. 6, U89–U101.

Popov, M. M., 2002, Ray theory and Gaussian beam method for geophysicists: EDUFBA.

Press, W. H., S. A. Teukolsky, W. T. Vetterling, and B. P. Flannery, 2007, Numerical recipes: The art of scientific computing: Cambridge University Press.

Robein, E., 2003, Velocities, time-imaging and depth-imaging in reflection seismics: EAGE.

Sethian, J., 1999, Fast marching methods: SIAM Review, **41**, 199–235.

Sethian, J. A., and A. M. Popovici, 1999, 3-D imaging using higher order fast marching traveltimes: Geophysics, **64**, 516–523.

Stork, C., and R. W. Clayton, 1992, Using constraints to address the instabilities of automated prestack velocity analysis: Geophysics, **57**, 404–419.

Tikhonov, A. N., 1963, Solution of incorrectly formulated problems and the regularization method: Sovet Math. Dokl., 1035–1038.

Červený, V., 2001, Seismic ray theory: Cambridge University Press.

Xu, S., H. Chauris, G. Lambaré, and M. Noble, 2001, Common-angle migration: A strategy for imaging complex media: Geophysics, **66**, 1877–1894.

Yilmaz, O., 2001, Seismic data analysis: SEG.

Yilmaz, O., I. Tanir, and C. Gregory, 2001, A unified 3-d seismic workflow: Geophysics, **66**, 1699–1713.

Zhdanov, M., 2002, Geophysical inverse theory and regularization problems: Elsevier

Science.